

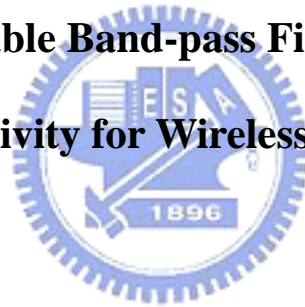
國立交通大學

電信工程學系碩士班

碩士論文

應用於無線通訊系統之電子式可調帶通濾波器

The Electrically Tunable Band-pass Filter with Compact Size and  
High Selectivity for Wireless Communication



研究生：黃正宏

指導教授：彭松村 博士

黃瑞彬 博士

中華民國九十三年七月

# **The Electrically Tunable Band-pass Filter with Compact Size and High Selectivity for Wireless Communication**

研 究 生：黃正宏

**Student: Cheng-Hung Huang**

指 導 教 授：彭松村 博士

**Advisor: Dr. Song-Tsuen Peng**

黃瑞彬 博士

**Dr. Ruey-Bing Hwang**

國 立 交 通 大 學

電 信 工 程 學 系 碩 士 班



**Submitted to Department of Communication Engineering**

**College of Electrical Engineering and Computer Science**

**National Chiao Tung University**

**In partial Fulfillment of the Requirements**

**for the Degree of**

**Master of Science**

**in**

**Electrical Engineering**

**July 2004**

**Hsinchu, Taiwan, Republic of China**

中 華 民 國 九 十 三 年 七 月

# 應用於無線通訊系統之電子式可調帶通濾波器


研 究 生：黃正宏

指導教授：彭松村 博士

黃瑞彬 博士

國立交通大學電信工程學系碩士班

## 中文摘要



在這篇論文中，我們發展了一個電子式可調帶通濾波器，這濾波器由開迴路環形共振器和 varactor 所構成。我們經由電路模擬來計算帶通濾波器的介入和反射損失，此外，我們也完成了實驗，且由模擬和量測相近的結果，我們更可確定電路模型的正確性。另外，在共振器上的 varactor 是用來調整共振器的共振頻率，如預期的，由 varactor 所造成的電抗確實的影響到共振器的總電感和電容值，值得一提的是，不僅濾波器的中心頻率可以被改變，這電抗是電感性或是電容性也將決定濾波器的中心頻率將大於或小於未加 varactor 時濾波器的中心頻率，利用這個結果，我們也實現了一個寬的可調頻率帶通濾波器，雖然不理想之二極體的 Q 值增加了濾波器的介入損失，但這原理是被證明可有效的用於調變帶通濾波器的中心頻率。

# **The Electrically Tunable Band-pass Filter with Compact Size and High Selectivity for Wireless Communication**

Student: Cheng-Hung Huang

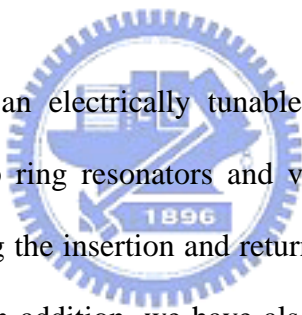
Advisor: Dr. Song-Tsuen Peng

Dr. Ruey Bing Hwang

Department of Communication Engineering

National Chiao-Tung University

## Abstract

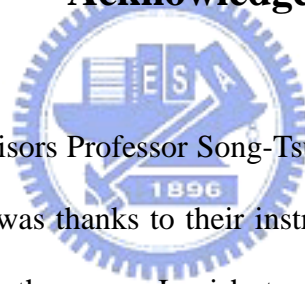
The logo of National Chiao-Tung University is a circular emblem. It features a gear-like outer border. Inside the circle, there is a stylized representation of a building or a bridge structure. At the bottom of the inner circle, the year '1896' is inscribed.

In this thesis, we developed an electrically tunable band-pass filter. The filter contains multiple sections of open-loop ring resonators and varactors. For the band-pass filter, the scattering parameters, including the insertion and return losses, has been calculated by means of electric circuit simulation. In addition, we have also carried out the experimental studies. The excellent agreements between simulated and measured results prove the accuracy of the established circuit model. Moreover, the varactor was added to the resonator to adjust its resonant frequency. As expected, the reactance introduced by the varactor indeed affects the net inductance and capacitance obviously. It is noted that, not only the shift with the center frequency, the inductive or capacitive of the reactance can also provide a parameter to switch its frequency toward the two directions away from the one without varactor. As a consequence, a wideband tunable band-pass filter is achieved. Although the bad quality factor with the diode strongly increases the insertion loss, this concept was proved to be available for effectively tuning the center frequency of such a class of band-pass filter.

## 誌謝

我要感謝我的指導教授彭松村 教授、黃瑞彬 教授和實驗室同伴們，感謝他們的教導與幫忙，這篇論文才可以順利的完成，另外我們要感謝我的家人們，感謝他們長期對我的支持與鼓勵，最後，謹將此篇論文獻給我的父母，感謝他們多年來的辛苦栽培。

## Acknowledgement



I would like to thank my advisors Professor Song-Tsuen Peng, Professor Ruey Bing Hwang and my partners of the lab. It was thanks to their instruction and help that this thesis can be accomplished successfully. Furthermore, I wish to thank my family for that they have supported and encouraged me for a long time. In the final, I would like to donate this thesis to my parents, and thank their hard nurture for many years.

# CONTENTS

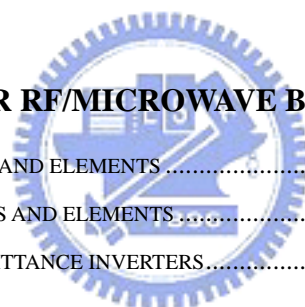
CHINESE ABSTRACT .....	I
ENGLISH ABSTRACT .....	II
ACKNOWLEDGMENT .....	III
CONTENTS .....	IV
LIST OF FIGURES AND TABLES .....	VI

## CHAPTER 1

INTRODUCTION .....	1
--------------------	---

## CHAPTER 2

THE BASIC CONCEPT FOR RF/MICROWAVE BAND-PASS FILTER.....	3
2.1 LOW-PASS PROTOTYPE FILTERS AND ELEMENTS .....	4
2.2 BAND-PASS PROTOTYPE FILTERS AND ELEMENTS .....	6
2.3 BAND-PASS FILTERS WITH ADMITTANCE INVERTERS.....	7



## CHAPTER 3

THE EXTERNAL QUALITY FACTOR DESIGN CURVES AND COUPLING COEFFICIENT DESIGN CURVES.....	11
3.1 THE OPEN-LOOP RING RESONATOR .....	11
3.2 QUALITY FACTOR DESIGN CURVES .....	14
3.3 COUPLING COEFFICIENT DESIGN CURVES .....	18
3.3.1 electric coupling and magnetic coupling structures .....	19
3.3.2 electric coupling design curves.....	20
3.3.3 magnetic coupling coefficient design curves.....	24

## CHAPTER 4

PRACTICAL REALIZATION OF THE BAND-PASS FILTER FOR MICROSTRIP...	28
4.1 THE BAND-PASS FILTER WITH SYMMETRIC FEED LINES .....	28
4.2 THE BAND-PASS FILTER WITH ASYMMETRIC FEED LINES .....	30

**CHAPTER5**

**THE DESIGN METHOD AND PRACTICAL REALIZATION OF THE NEW  
TUNABLE BAND-PASS FILTERS .....37**

- 5.1 THE MECHANISM OF FREQUENCY TUNING ..... 37
- 5.2 THE TUNABLE BAND-PASS FILTER USING CAPACITANCE REACTANCE X ..... 40
- 5.3 THE TUNABLE BAND-PASS FILTER USING INDUCTANCE REACTANCE X..... 46
- 5.4 THE BAND-PASS FILTER HAVING WIDE TUNABLE BANDWIDTH ..... 49

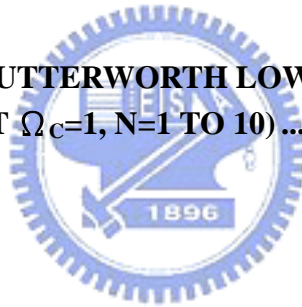
**CHAPTER6**

**CONCLUSION .....53**

**REFERENCE .....54**

**APPENDIX A**

**ELEMENT VALUES FOR BUTTERWORTH LOW-PASS FILTER ROTOTYPES  
( $G_0=1, \Omega_C=1, L_{AR}=3.01DB$  AT  $\Omega_C=1, N=1$  TO 10) .....56**



# List of Figures and Tables

<b>FIGURE 2.1</b> THE LADDER CIRCUITS FOR LOW-PASS FILTER PROTOTYPES AND THEIR ELEMENT DEFINITIONS .....	3
<b>FIGURE 2.2</b> THE LADDER LC LUMP CIRCUITS FOR LOW-PASS FILTER PROTOTYPES AND THEIR LUMP VALUE DEFINITIONS.....	5
<b>FIGURE 2.3</b> THE LADDER LC LUMP CIRCUITS FOR BAND-PASS FILTER PROTOTYPES AND THEIR LUMP VALUE DEFINITIONS.....	6
<b>FIGURE 2.4</b> BAND-PASS FILTERS USING ADMITTANCE INVERTERS .....	7
<b>FIGURE 2.5</b> ADMITTANCE INVERTERS USED TO CONVERT A SERIES INDUCTANCE INTO AN EQUIVALENT .....	8
<b>FIGURE 3.1</b> A PARALLEL GLC RESONANT CIRCUIT .....	12
<b>FIGURE 3.2</b> A <b>HALF-WAVELENGTH</b> OPEN-LOOP MICROSTRIP RING RESONATOR .....	13
<b>FIGURE 3.3</b> A <b>HALF-WAVELENGTH</b> OPEN-LOOP MICROSTRIP RING RESONATOR THAT CONSIDERS EFFECT OF THE GAP .....	13
<b>FIGURE 3.4</b> THE CIRCUIT RESPONSES OF IMPEDANCE MAGNITUDE VERSUS FREQUENCY FOR <b>FIGURE 3.1</b> A PARALLEL GLC RESONANT CIRCUIT .....	15
<b>FIGURE 3.5</b> THE RESONANCE CIRCUIT THAT IS COUPLED TO THE SOURCE RESISTANCE $R_S$ . ....	15
<b>FIGURE 3.6</b> PHASE RESPONSE OF $S_{11}$ FOR THE CIRCUIT IN FIGURE 3.5.....	17
<b>FIGURE 3.7</b> A HALF-WAVELENGTH OPEN-LOOP RING RESONATOR WITH A FEED LINE.....	17
<b>FIGURE 3.8</b> THE DESIGN CURVES OF $Q_E$ FOR AN OPEN-LOOP RING MICROSTRIP BAND-PASS FILTER OBTAINED BY CIRCUIT SIMULATION .....	18
<b>FIGURE 3.9</b> TYPICAL COUPLING STRUCTURES OF COUPLED MICROSTRIP SQUARE OPEN-LOOP RESONATORS (A) ELECTRIC COUPLING STRUCTURE. (B) MAGNETIC COUPLING STRUCTURE. ..	19
<b>FIGURE 3.10</b> (A) AN EQUIVALENT LUMPED-ELEMENT CIRCUIT OF ELECTRIC COUPLING STRUCTURE (B) AN ALTERNATIVE FORM OF THE EQUIVALENT CIRCUIT WITH AN ADMITTANCE INVERTER .....	21
<b>FIGURE 3.11</b> THE $S_{21}$ RESPONSES FOR THE ELECTRIC STRUCTURE WHEN THE COUPLED RESONATOR CIRCUITS ARE OVER-COUPLED .....	23
<b>FIGURE 3.12</b> THE COUPLING COEFFICIENT CURVE FOR THE ELECTRIC COUPLED RESONATOR	



STRUCTURE.....	23
<b>FIGURE3.13</b> (A) AN EQUIVALENT LUMPED-ELEMENT CIRCUIT OF MAGNETIC COUPLING STRUCTURE (B) AN ALTERNATIVE FORM OF THE EQUIVALENT CIRCUIT WITH AN IMPEDANCE INVERTER .....	25
<b>FIGURE 3.14</b> THE $S_{21}$ RESPONSES FOR THE MAGNETIC COUPLING STRUCTURE WHEN THE COUPLED RESONATOR CIRCUITS ARE OVER-COUPLED .....	26
<b>FIGURE 3.15</b> THE COUPLING COEFFICIENT CURVE FOR THE MAGNETIC COUPLED RESONATOR STRUCTURE.....	27
<b>FIGURE 4.1</b> THE OPEN-LOOP RING BAND-PASS FILTER WITH THE SYMMETRIC FEED LINES.....	29
<b>FIGURE4.2</b> THE $S_{21}$ OF SIMULATION AND MEASUREMENT FOR THE OPEN-LOOP RING BAND-PASS FILTER WITH THE SYMMETRIC FEED LINES .....	29
<b>FIGURE4.3</b> THE $S_{11}$ OF SIMULATION AND MEASUREMENT FOR THE OPEN-LOOP RING BAND-PASS FILTER WITH THE SYMMETRIC FEED LINES .....	30
<b>FIGURE 4.4</b> THE FILTER USING TWO HAIRPIN RESONATORS WITH ASYMMETRIC TAPPING FEED LINES .....	31
<b>FIGURE 4.5</b> THE OPEN-LOOP RING BAND-PASS FILTER WITH THE ASYMMETRIC FEED LINES ....	33
<b>FIGURE4.6</b> THE $S_{21}$ OF SIMULATION AND MEASUREMENT FOR THE OPEN-LOOP RING BAND-PASS FILTER WITH THE ASYMMETRIC FEED LINES.....	33
<b>FIGURE4.7</b> THE $S_{11}$ OF SIMULATION AND MEASUREMENT FOR THE OPEN-LOOP RING BAND-PASS FILTER WITH THE ASYMMETRIC FEED LINES.....	34
<b>FIGURE 4.8</b> THE $S_{21}$ OF MEASUREMENT FOR THE OPEN-LOOP RING BAND-PASS FILTER WITH THE SYMMETRIC AND ASYMMETRIC FEED LINES.....	34
<b>FIGURE4.9</b> THE LAYOUT OF THE FILTER USING FOUR CASCADED OPEN-LOOP RING RESONATORS WITH THE ASYMMETRIC FEED LINES.....	35
<b>FIGURE4.10</b> THE MEASURED RESULTS OF THE FILTER USING FOUR CASCADED OPEN-LOOP RING RESONATORS WITH ASYMMETRIC FEED LINES.....	36
<b>FIGURE 5.1</b> THE CONVENTIONAL STRUCTURE FOR THE ELECTRICALLY TUNABLE FREQUENCY RESONATOR .....	39
<b>FIGURE 5.2</b> THE EQUIVALENT CIRCUIT FOR THE VARACTOR CONNECT THE VIA HOLE GROUND (A) CONSIDERING THE PARASITIC EFFECTS OF THE PACKAGE (B) NEGLECTING THE PARAMETER $C_p$ AND $R_s$ .....	39
<b>FIGURES5.3</b> THE NEW STRUCTURE FOR THE ELECTRICALLY TUNABLE FREQUENCY RESONATOR .....	40

<b>FIGURE 5.4</b> THE MEASUREMENT CIRCUIT FOR $L_T$ .....	<b>40</b>
<b>FIGURE 5.5</b> THE SIMULATED RESPONSES FOR $C_T$ AND $X$ VERSUS $F_0$ .....	<b>41</b>
<b>FIGURE 5.7</b> THE LAYOUT OF THE NEW TUNABLE BAND-PASS FILTER .....	<b>42</b>
<b>FIGURE 5.8</b> THE SIMULATION OF THE TUNABLE BAND-PASS FILTER WITH THE CAPACITANCE REACTANCE $X$ AND THE $BW= 50\text{MHZ}$ .....	<b>43</b>
<b>FIGURES.9</b> THE MEASUREMENT OF THE TUNABLE BAND-PASS FILTER WITH THE CAPACITANCE REACTANCE $X$ AND THE $BW= 50\text{MHZ}$ .....	<b>43</b>
<b>FIGURES.10</b> THE MEASUREMENT OF THE TUNABLE BAND-PASS FILTER WITH THE CAPACITANCE REACTANCE $X$ AND THE $BW= 100\text{MHZ}$ .....	<b>44</b>
<b>FIGURE 5.11</b> THE RESPONSE CURVES FOR THE $D_1$ AGAINST THE RESONANT FREQUENCY.....	<b>46</b>
<b>FIGURE 5.12</b> THE SIMULATION OF THE TUNABLE BAND-PASS FILTER WITH THE INDUCTANCE REACTANCE $X$ .....	<b>47</b>
<b>FIGURES.13</b> THE MEASUREMENT OF THE TUNABLE BAND-PASS FILTER WITH THE INDUCTANCE REACTANCE $X$ .....	<b>48</b>
<b>FIGURE 5.14</b> THE CIRCUIT OF THE WIDE TUNABLE BAND-PASS FILTER WITH $N$ SWITCHES OF EACH BRANCH OF THE RING .....	<b>50</b>
<b>FIGURES.15</b> THE SIMULATION OF THE WIDE TUNABLE BAND-PASS FILTER FOR ONE SWITCH OF EACH BRANCH OF THE RING .....	<b>51</b>
<b>FIGURE 5.16</b> THE MEASUREMENT OF THE WIDE TUNABLE BAND-PASS FILTER FOR ONE SWITCH OF EACH BRANCH OF THE RING .....	<b>51</b>
<b>TABLE5-1</b> THE SIMULATION AND MEASUREMENT RESULTS OF THE TUNABLE BAND-PASS FILTER WITH THE CAPACITANCE REACTANCE .....	<b>45</b>
<b>TABLE5-2</b> THE SIMULATION AND MEASUREMENT RESULTS OF THE TUNABLE BAND-PASS FILTER WITH THE INDUCTANCE REACTANCE.....	<b>48</b>
<b>TABLE5-1</b> THE SIMULATION AND MEASUREMENT RESULTS OF THE TUNABLE BAND-PASS FILTER FOR ONE SWITCH OF EACH OF THE RING .....	<b>52</b>

# Chapter 1

## Introduction

The characteristics of high selectivity, compact size and tunable frequency for modern microwave and millimeter wave filters are highly required for the next generation mobile and satellite communication systems. However, a band-pass filter having these characteristics together in the realization is not easy to achieve. In this work, the design and realization of the tunable band-pass filter with high selectivity, small size and tunable frequency will be presented.

The design methodology of a LC lumped-element filter with butterworth response has been popularly employed. However, two problems arise at microwave frequencies. First, lumped elements such as inductors and capacitors are, in general, available only for a limited range of values and are difficult to implement at microwave frequencies, thus the distributed components are needed to obtain more precise circuit model. In addition, at microwave frequencies the distances between filter components are considerable. Thus, in this thesis, we introduce a filter design methodology using microstrip-line resonator and coupled transmission-line [1].

Using the cross-coupled planar microwave filters have a characteristic of high selectivity [2], but they often need at least four resonators and show a high insertion loss [3][4]. Recently, the method of increasing selectivity for filter, however, without increasing its size was proposed by [5]. This method employ the asymmetric feed to produce two transmission zeros in its response. Moreover, since the two zeros locate at the two pass-band edges, it could further enhance the selectivity of the filter. In chapter 4, we verify the method described previously by using numerical simulation and experimental studies both.

In addition, a reconfigurable scheme is incorporated with such a high selectivity and small size filter to achieve purpose of tunable filter design.

Most tunable filters described in the literature are classified into three categories: mechanically tunable, magnetically tunable, and electronically tunable filters [6]. However electronically tunable filters have the characteristics of high-speed tuning over a wide tuning range, and are compact in their size, such as, GaAs varactor diodes [7][8], MESFETs [9] or PET. Although some conventional electrically tunable filters having the advantage of high-speed tuning and small size were reported [10][11], in chapter5 we will propose some new schemes of tunable filters which have small size and wide tunable frequency range and a higher selectivity based on asymmetric feed lines. Beside, by tapping the position of the varactor or switch, the filters have another advantage, that it can compensate that the values of  $C_T$  and  $L_T$  to achieve the impedance match. As a result, it provides many possibilities in choosing the devices.

In chapter 4 and chapter 5, the some simulations and measurements of the filters are presented. In the numerical simulation, we use Microwave Office software<sup>TM</sup>, HP 8722D network analyzer for measuring the return- and insertion-losses of the filters.

# Chapter 2

## The basic concept for RF/microwave band-pass filter

This chapter describes some basic concepts for the design of general RF/microwave band-pass filters. The topics to be cover of include: low-pass prototype filters and elements, band-pass prototype filters and elements, and band-pass filters with admittance inverters.

### 2.1 Low-pass prototype filters and elements

The prototype by a low-pass filter is, in general, defined that whose element values are normalized, such that the source resistance or conductance is equal to unity ( $g_0 = 1$ ), and so is the cutoff angular frequency ( $\Omega_c = 1$ ). Figure 2.1 depicts a ladder network for use as a low-pass filter with their elements attached [12]. Here,  $g_0$  and  $g_{n+1}$  are defined as the source and load resistance, respectively, and the  $g_i$ , for  $i = 1$  to  $n$ , stand for the series inductors or shunt capacitors, where  $n$  is the number of reactive elements.

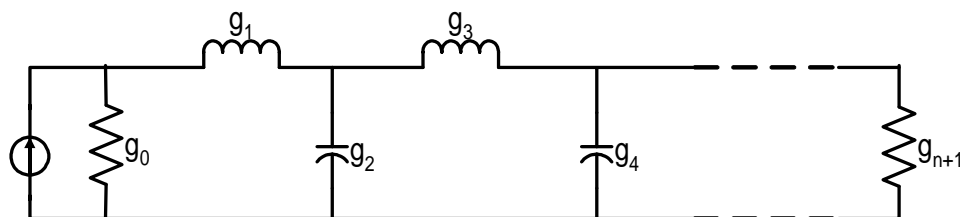


**Figure 2.1** The ladder circuits for low-pass filter prototypes and their element definitions

In the procedures for filter design for the Butterworth low-pass prototype with insertion loss  $L_{Ar}=3.01\text{dB}$  at the unit cutoff angular frequency  $\Omega_c = 1$ , the values of elements in figure 2.1 may be computed [13] by

$$g_0 = 1 \quad (2.1)$$

$$g_i = 2 \sin\left(\frac{(2i-1)\pi}{2n}\right) \quad , \text{for } i=1,2,3,\dots,n \quad (2.2)$$

$$g_{n+1} = 1 \quad (2.3)$$

, Furthermore, for convenient references, Appendix A gives some typical element values for such filters having  $n = 1$  to 10. It is noted that a modified Butterworth response such as Chebyshev response may also be used to design a low-pass prototype filter as that in Figure 2.1 [13].

In the prototype design, not only the element values ( $g_i$ ) are normalized to the source resistance  $R_0$ , but also the frequency  $\Omega$  is normalized to by  $\omega$ . In order to obtain the actual frequency response and element values for practical filters based on the low-pass prototype, the impedance and frequency transformations are needed; they are given by:

$$R_s = \frac{1}{G_s} = R_0 \quad (2.4)$$

$$L_i = g_i R_0 \quad , \text{for } g \text{ representing the inductance} \quad (2.5)$$

$$C_i = \frac{g_i}{R_0} \quad , \text{for } g \text{ representing the capacitance} \quad (2.6)$$

$$R_L = \frac{1}{G_L} = g_{n+1} R_0 \quad (2.7)$$

For the low-pass filter of the cutoff frequency  $\omega_c$ , the frequency transformation is

$$\omega = \Omega \omega_c \quad (2.8)$$

where  $R_s$  ( $G_s$ ) and  $R_L$  ( $G_L$ ) are the source impedance (admittance) and the load impedance (admittance), respectively.  $\omega_c$  is the cutoff angular frequency of the filter. Combining impedance transforms (2.4) to (2.7) together with frequency transforms (2.8) [13], the element transformations can be written as

$$L'_i = \frac{L_i}{\omega_c} = \frac{R_0 g_i}{\omega_c}, \text{ for } g_i \text{ representing the inductance} \quad (2.9)$$

$$C'_i = \frac{C_i}{\omega_c} = \frac{g_i}{R_0 \omega_c}, \text{ for } g_i \text{ representing the capacitance} \quad (2.10)$$

Invoking (2.4), (2.7), (2.9) and (2.10) into the elements in Figure 2.1 can be transformed into those in Figure 2.2. Thus, the Butterworth low-pass filter consisting of LC lump elements can be so designed without any difficulty.

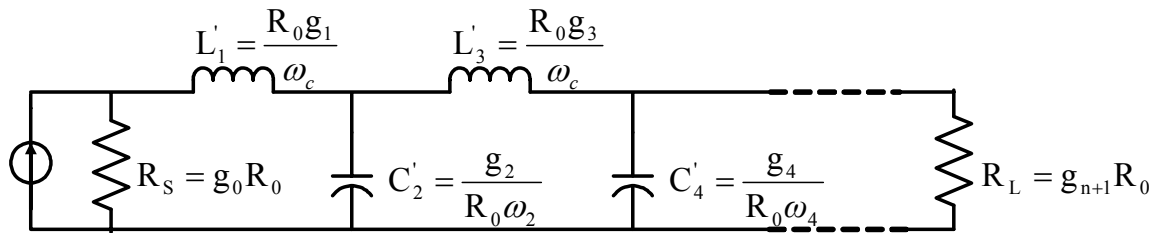


**Figure 2.2** The ladder LC lump circuits for low-pass filter prototypes and their lump value definitions



## 2.2 Band-pass prototype filters and elements

The design of band-pass filters that is a similar design rule of low-pass filters can also use the impedance and frequency transformations described previously. The impedance transformations of the band-pass filter are equivalent to the low-pass filter such as (2.4 ~ 2.7), but the frequency transformation of the band-pass filter is different from the low-pass filter [13]. It is

$$\Omega = \frac{1}{\text{FBW}} \left( \frac{\omega}{\omega_0} - \frac{\omega_0}{\omega} \right) \quad (2.11)$$

$$\text{FBW} = \frac{\omega_2 - \omega_1}{\omega_0}; \omega_0 = \sqrt{\omega_1 \omega_2} \quad (2.12)$$

Here FBW is the fractional bandwidth,  $\omega_0$  is the center angular frequency of pass band,  $\omega_1$ ,  $\omega_2$  denote the edges of the passband. When this frequency transformation is applied to reactive element  $g$  of the low-pass prototype, an inductive/capacitive element  $g$  in the low-pass prototype will transform to a series/parallel LC resonant circuit in the band-pass filter. In [13], the element transformations for the series and parallel resonator in the band-pass filter are written below

$$L'_i = \left( \frac{1}{\text{FBW} \omega_0} \right) R_0 g_i \quad \text{for } g_i \text{ presenting the inductance and } \Omega_c = 1 \quad (2.13)$$

$$C'_i = \frac{1}{\omega_0^2 L'_i} = \left( \frac{\text{FBW}}{\omega_0} \right) \frac{1}{R_0 g_i} \quad \text{for } g_i \text{ presenting the inductance and } \Omega_c = 1 \quad (2.14)$$

$$C'_i = \left( \frac{1}{\text{FBW} \omega_0} \right) \frac{g_i}{R_0} \quad \text{for } g_i \text{ presenting the capacitance and } \Omega_c = 1 \quad (2.15)$$

$$L'_i = \frac{1}{\omega_0^2 C'_i} = \left( \frac{\text{FBW}}{\omega_0} \right) \frac{R_0}{g_i} \quad \text{for } g_i \text{ presenting the capacitance and } \Omega_c = 1 \quad (2.16)$$

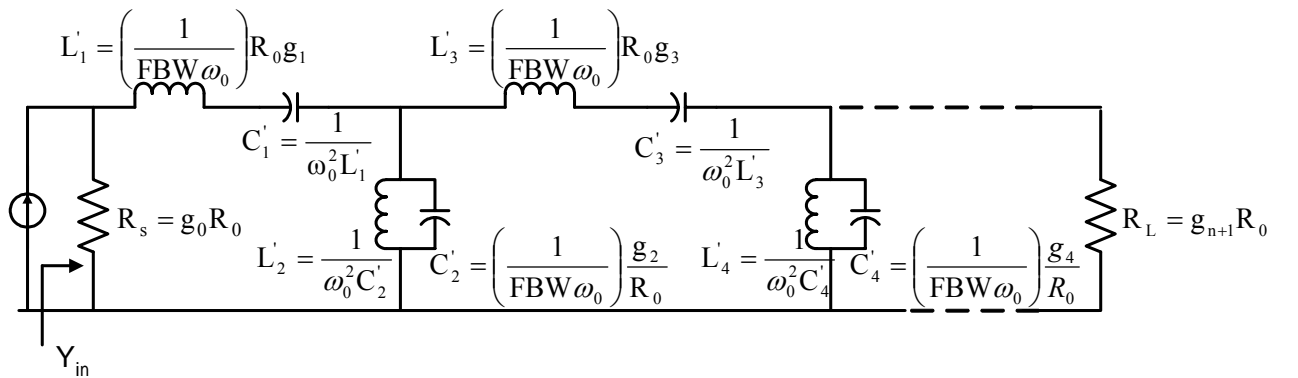


**Figure 2.3** The ladder LC lump circuits for band-pass filter prototypes and their lump value definitions

Adopting the element transformations from (2.13) to (2.16) and impedance transformations (2.4) and (2.7), the low-pass filter in Figure 2.1 can be easily transformed into a band-pass



filter indicated in Figure 2.3. The transformation method allows us to transform the prototype filter.

## 2.3 Band-pass filters with admittance inverters

The band-pass filter structure in Figure 2.3 consists of series resonators alternating with shunt resonators with discrete components, but the arrangement is difficult to implement with planar structures for high frequency applications. In practice, it is much more practical to use a structure which approximates the circuit in Figure 2.4, where the J's stand for the admittance inverters. An ideal admittance inverter is a two-port network that has a unique property at all frequencies, to transform a shunt-connected element to a series-connected element. Specifically, if the admittance  $Y_2$  is connected at one port of the admittance inverters, the admittance  $Y_1$  seen at the other port of the admittance inverters is

$$Y_1 = \frac{J^2}{Y_2} \quad (2.17)$$

In general, an ideal admittance inverter has the ABCD matrix is given by:

$$\begin{bmatrix} A & B \\ C & D \end{bmatrix} = \begin{bmatrix} 0 & \pm \frac{1}{jJ} \\ \mp jJ & 0 \end{bmatrix} \quad (2.18)$$

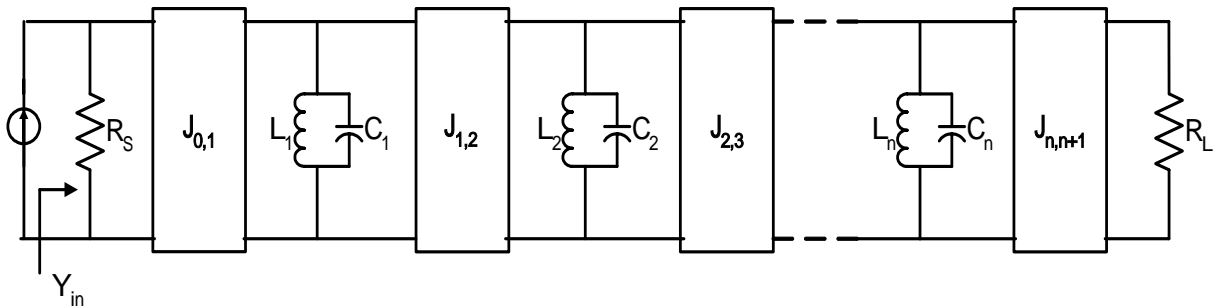


**Figure 2.4** Band-pass filters using admittance inverters

As a simple example to show the function of admittance inverters, a parallel resonator with an admittance inverter on each side is equivalent to a series resonator, as illustrated in Figure 2.5.

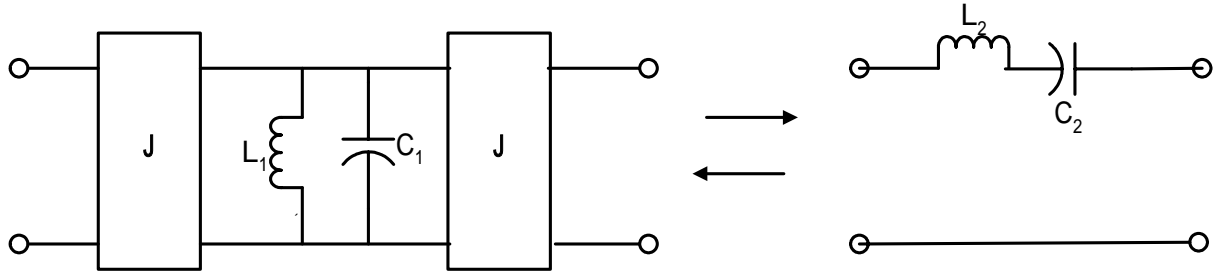


**Figure 2.5** Admittance inverters used to convert a series resonator into an equivalent circuit with parallel resonator

If the parameters in (2.17) and (2.18) are substituted into those in Figure 2.4 and thus  $Y_{in}$  in Figure 2.3 and 2.4 are equivalent, under the condition of  $\Omega_c = 1$ , and the admittance-inverter values are

$$J_{0,1} = \sqrt{\frac{FBW\omega_0 C_1}{g_0 g_1 R_0}} \quad (2.19)$$

$$J_{i,i+1} = FBW\omega_0 \sqrt{\frac{C_i C_{i+1}}{g_i g_{i+1}}}, i = 1 \text{ to } n - 1 \quad (2.20)$$

$$J_{n,n+1} = \sqrt{\frac{FBW\omega_0 C_n}{g_n g_{n+1} R_L}} \quad (2.21)$$

In the structure of Figure 2.4, all the resonators are of the same type, so that, the frequency response is the same as that in Figure 2.3. Notice that the structure in Figure 2.4 is more practical than that of Figure 2.3 for designing the microwave band-pass filters. Besides, the resonators used in microwave system are generally distributed not lumped, to replace the lumped LC resonators by distributed circuits, such as: distributed circuits can be microwave

cavities, microstrip resonators, or any other suitable resonant structures. We have to make certain the accuracy of the circuit models.

Furthermore, the external Q and the coupling coefficient k are defined as

$$Q_e = \frac{B}{G_0} \quad (2.22)$$

$$k_{i,i+1} = \frac{L_{i,i+1}}{\sqrt{L_i L_{i+1}}} = \frac{C_{i,i+1}}{\sqrt{C_i C_{i+1}}} = \frac{J_{i,i+1}}{\omega \sqrt{C_i C_{i+1}}} \quad (2.23)$$

where,  $G_0$  is external load inductance,  $B$  is the susceptance of the resonator,  $L_{i,i+1}$  is the mutual inductance,  $L_i$  and  $L_{i+1}$  are self inductance,  $C_{i,i+1}$  is the mutual capacitance,  $C_i$  and  $C_{i+1}$  are self capacitance [1]. Substituting (2.19) (2.20) (2.21) into (2.22) (2.23), the equation (2.22) (2.23) can be rewritten as below:

$$Q_{e1} = \frac{g_0 g_1}{FBW} \quad (2.24)$$

$$k_{i,i+1} = \frac{FBW}{\sqrt{g_i g_{i+1}}}, \text{ for } i = 1 \text{ to } (n-1) \quad (2.25)$$

$$Q_{en} = \frac{g_n g_{n+1}}{FBW} \quad (2.26)$$

, (2.24) to (2.26) are generalized equations for designing a band-pass filter only employing shunt-type resonators. The coupling coefficients  $k_{i,i+1}$  is a generalization of the usual definition of coupling coefficient between the adjacent resonators, the  $Q_{e1}$  is the external quality factor of the resonators at the input, and  $Q_{en}$  is the external quality factor of the resonators at the output.

Finally, we list the steps for designing a band-pass filter having merely parallel resonators, given below:

1. Determine the required order  $n$
2. The element values ( $g_i$ ) of a low-pass prototype filter for Butterworth response can be found from equation (2.1) to (2.3) or Appendix A

3. Determine the fractional bandwidth FBW and center frequency angular  $\omega_0$
4. Using equation (2.24) (2.25) and (2.26) to obtain the required parameters  $Q_{e_i}, k_{i,i+1}, Q_{en}$  of the band-pass filter only adopting parallel resonators.
5. Using distributed circuit to model the resonant circuit in step 4 above.

That practical realization of the band-pass filter in microwave will be discussed in the succeeding chapters.

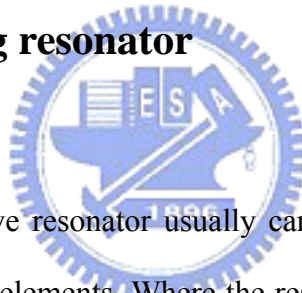


# Chapter 3

## The external quality factor design curves and coupling coefficient design curves

In the preceding chapter we had outlined the steps for designing practical band-pass filters which employ only parallel resonators in microwave. In this chapter we not only verify that a half wavelength open loop of microstrip indeed is a parallel resonator, but also discuss the method for refining the external quality factor design curves and coupling coefficient.

### 3.1 The open-loop ring resonator



Near resonance, a microwave resonator usually can be modeled by an equivalent circuit series or parallel RLC lumped-elements. Where the resistor (R) is the resonator's loss and, if the resonator is lossless, the R vanishes. Now, an opened-loop half-wavelength ring microstrip line can be modeled by a parallel RLC lumped-element equivalent circuit, which will be derived as follows.

Figure 3.1 shows a parallel RLC resonant circuit. The input admittance is

$$Y_{in} = \frac{1}{R} + j\omega C + \frac{1}{j\omega L} \quad (3.1)$$

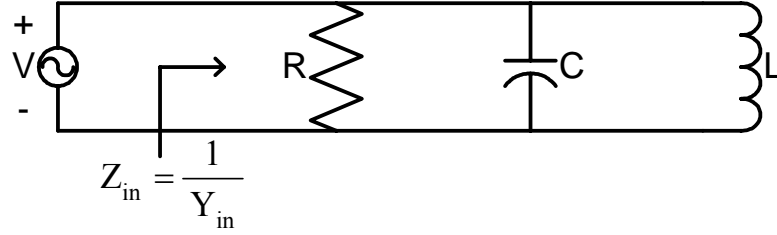


**Figure 3.1** A parallel GLC resonant circuit

Now consider the behavior of the input admittance of this resonator near its resonant frequency. Letting  $\omega = \omega_0 + \Delta\omega$ , where  $\omega_0$  is resonant angular frequency and  $\Delta\omega$  is small compared to  $\omega_0$ , such that (3.1) can be written to

$$\begin{aligned}
 Y_{in} &= \frac{1}{R} + j(\omega_0 + \Delta\omega)C + \frac{1}{j(\omega_0 + \Delta\omega)L} \\
 &= \frac{1}{R} + j(\omega_0 + \Delta\omega)C + \frac{1}{j\omega_0 L} \frac{1}{1 + \frac{\Delta\omega}{\omega_0}}
 \end{aligned} \tag{3.2}$$

by using the result of Maclaurin expansion, thus (3.2) can be rewritten as

$$\begin{aligned}
 Y_{in} &\approx \frac{1}{R} + j(\omega_0 + \Delta\omega)C - j \frac{\omega_0 - \Delta\omega}{\omega_0^2 L} \\
 &\approx \frac{1}{R} + 2j\Delta\omega C
 \end{aligned} \tag{3.3}$$

Besides, Figure 3.2 illustrates an open-circuited half-wavelength microstrip ring resonator. Figure 3.3 is equivalent to Figure 3.2 but considering the gap effect. As seen in Figure 3.3,  $l$  is the physical length of the ring,  $C_g$  is the gap capacitance, and  $C_f$  is the fringe capacitance caused by fringe field at the both ends of the ring. If the gap size between two open ends of the ring is large, the effect of the gap capacitor  $C_g$  for the ring can be ignored, and also the fringe capacitance  $C_f$  usually is not considerable [14].

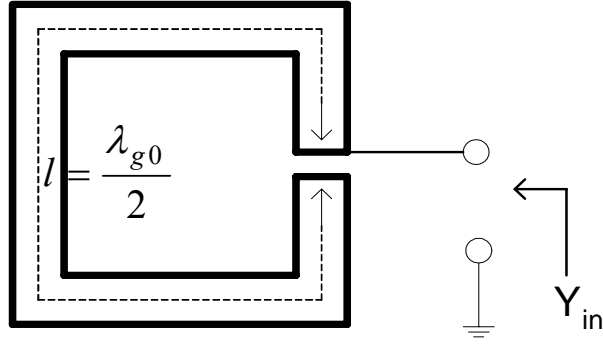


**Figure 3.2** A half-wavelength open-loop microstrip ring resonator

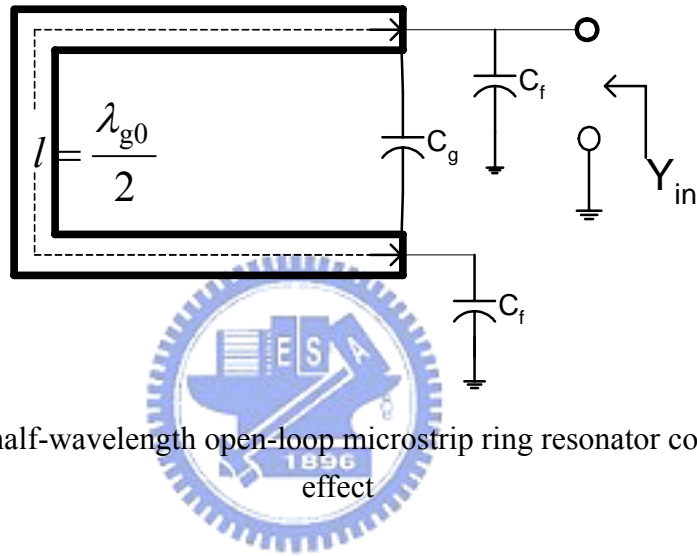


**Figure 3.3** A half-wavelength open-loop microstrip ring resonator considering the gap effect

Because both  $C_g$  and  $C_f$  are neglected, the input admittance in Figure 3.3 can be wrote as

$$Y_{in} = j \tan(\gamma l) \quad (3.4)$$

$$= \frac{1}{Z_0} \frac{\tanh(\alpha l) + j \tan(\beta l)}{1 + j \tanh(\alpha l) \tanh(\beta l)} \quad (3.5)$$

, where  $Z_0$  is characteristic impedance of the microstrip ring,  $\gamma$  is complex propagation constant,  $\alpha$  is the attenuation constant,  $\beta$  is the phase constant and  $\lambda_{g0}$  is the wavelength at

$\omega = \omega_0$ . Assume that  $l = \lambda_{g0} / 2$ , and let  $\omega = \omega_0 + \Delta\omega$ . Then,

$$\beta l = \pi + \frac{\pi \Delta\omega}{\omega_0},$$

$\tan(\beta l) = \tan(\Delta\omega\pi / \omega) \cong \Delta\omega\pi / \omega_0$ , and  $\tanh(\alpha l) \cong \alpha l$ . Using these results in (3.5) yields

$$Y_{in} \approx \frac{1}{Z_0} \alpha l + j \frac{\Delta \omega \pi}{Z_0 \omega_0} \quad (3.6)$$

Comparing (3.3) with (3.6), the input admittance of the opened-loop half-wavelength ring microstrip line has the same form as that of a parallel RLC circuit. Therefore, the capacitance in the equivalent circuit is

$$C = \frac{\pi}{2Z_0 \omega_0} \quad (3.7)$$

The inductance in the equivalent circuit can be obtained from  $\omega_0 = 1/\sqrt{LC}$  and is given by

$$L = \frac{1}{\omega_0^2 C} \quad (3.8)$$

and the resistance of the equivalent circuit is

$$R = \frac{Z_0}{\alpha l} = \frac{2Z_0}{\alpha \lambda_{g0}} \quad (3.9)$$

Moreover, the unloaded Q of the resonator denoted by  $Q_u$  is

$$Q_u = \frac{R}{\omega_0 L} = \frac{\pi}{2\alpha L} = \frac{\pi}{\alpha \lambda_{g0}} \quad (3.10)$$



## 3.2 Quality factor design curves

In the equation (3.10), The  $Q_u$  characterizes the resonant circuit itself, it doesn't include any loading effects for the external circuit, so it is named as the unload Q. Figure 3.4 shows the variation of impedance versus frequency for the circuit shown in Figure 3.1. In this figure, the  $\omega_1$  and  $\omega_2$  are the frequencies which make  $|Z_{in}|^2 = 2R^2$ . When the frequency at  $\omega_1$  and  $\omega_2$ , the average power delivered to the circuit is half that at resonance, and in this case, an unload Q of the circuit can be defined by equation (3.11) [12].



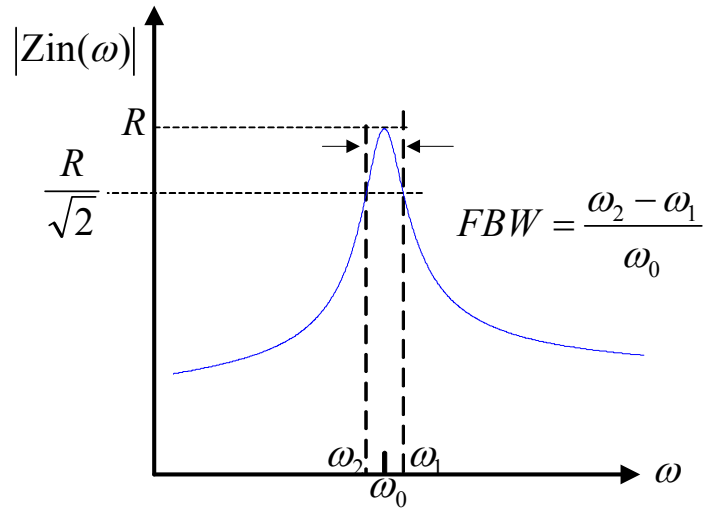


**Figure 3.4** The circuit responses of impedance magnitude versus frequency for Figure 3.1

$$Q_u = \frac{1}{FBW} \quad , \text{ for Figure 3.1 and Figure 3.4} \quad (3.11)$$

However, in practice, the resonant circuit always is coupled to other circuit such as Figure 3.5. It will reduce the Q factor of the circuit. This Q is called to load Q denoted as  $Q_L$  [12] which  $Q_e$  is called the external quality factor, the relationship among Q,  $Q_L$ , and  $Q_e$  are

$$\frac{1}{Q_u} = \frac{1}{Q_L} + \frac{1}{Q_e} \quad (3.12)$$

In the following section, we will introduce a method to carry out the calculation for the  $Q_e$ . Once the  $Q_e$  is determined, we can have the exact relation between  $Q_u$  and  $Q_e$ .

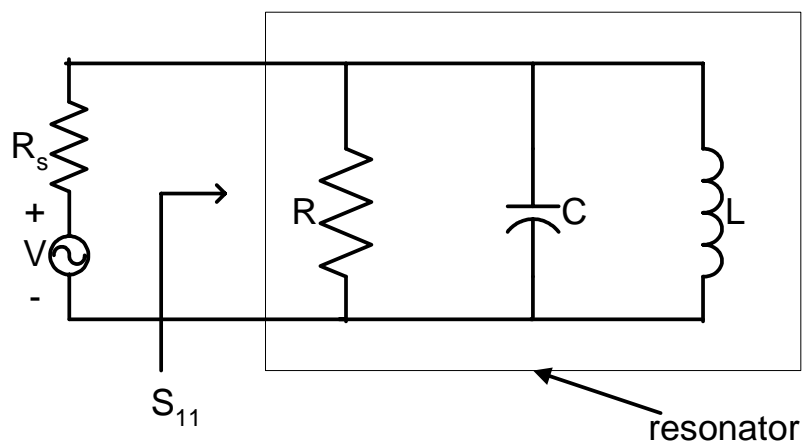


**Figure 3.5** The resonance circuit that is coupled to the source resistance  $R_s$ .

In Figure 3.5, the reflection coefficient or  $S_{11}$  and its phase at the excitation port can be approximated by equation (3.13) (3.14) [13].

$$S_{11} = \frac{1 - jQ_e(2\Delta\omega/\omega_0)}{1 + jQ_e(2\Delta\omega/\omega_0)} \quad (3.13)$$

$$\angle S_{11} = \tan^{-1}[-Q_e(2\Delta\omega/\omega_0)] - \tan^{-1}[Q_e(2\Delta\omega/\omega_0)] \quad (3.14)$$

In the equation (3.14), when  $\angle S_{11} = \pm 90^\circ$ ,  $2Q_e \frac{\Delta\omega_{\mp}}{\omega_0} = \mp 1$ . Hence, the absolute bandwidth between the  $\pm 90^\circ$  point is

$$\Delta\omega_{\pm 90^\circ} = \Delta\omega_+ - \Delta\omega_- = \frac{\omega_0}{Q_e} \quad (3.15)$$

, where  $\Delta\omega_{\mp}$ ,  $\Delta\omega_{\pm 90^\circ}$ ,  $\Delta\omega_+$  and  $\Delta\omega_-$  are indicated in Figure 3.6. The  $Q_e$  in (3.15) can be rewritten to:

$$Q_e = \frac{\omega_0}{\Delta\omega_{\pm 90^\circ}} \quad (3.16)$$

Equation (3.16) and Figure 3.6 provide a convenient method to calculate the  $Q_e$ , and thus, we can find the  $Q_e$  design curve of the circuit in Figure 3.7. Figure 3.8 is the design curves of  $Q_e$  obtained by circuit simulation for design of an open-loop ring microstrip band-pass filter. It is noted that the location  $t$  of the feed line will affect the external quality factor considerably. To systematically obtain the design curve for  $Q_e$ , we change progressively the distance  $t$  to calculate  $Q_e$  by numerical simulation. The variation of  $Q_e$  against distance  $t$  is shown in Figure 3.8. It can be considered as a look up table, that is, we can find out the  $Q_e$  by specifying the distance  $t$ , which is given by the designer.

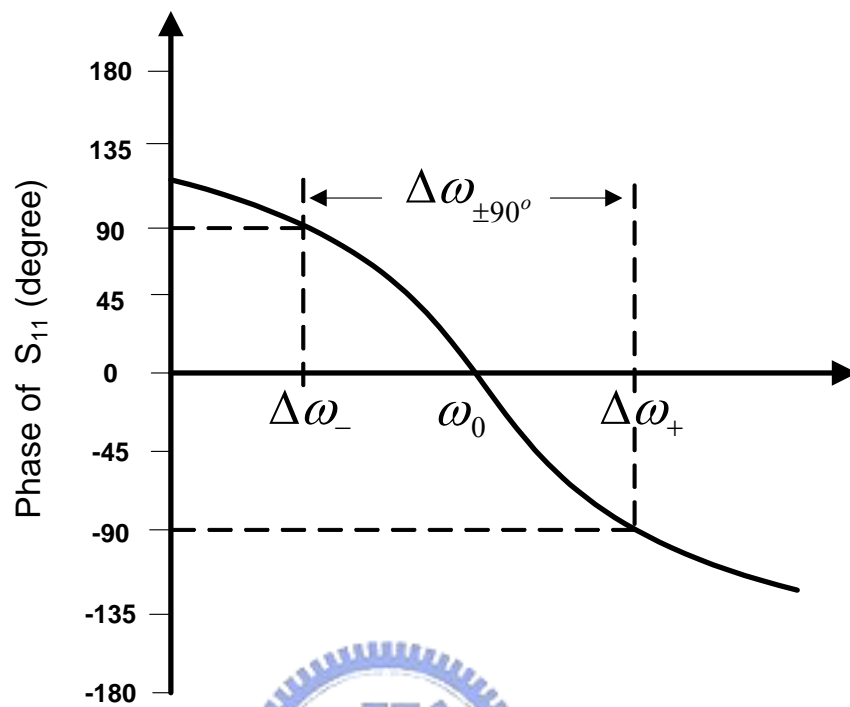


Figure 3.6 Phase response of  $S_{11}$  for the circuit in Figure 3.5

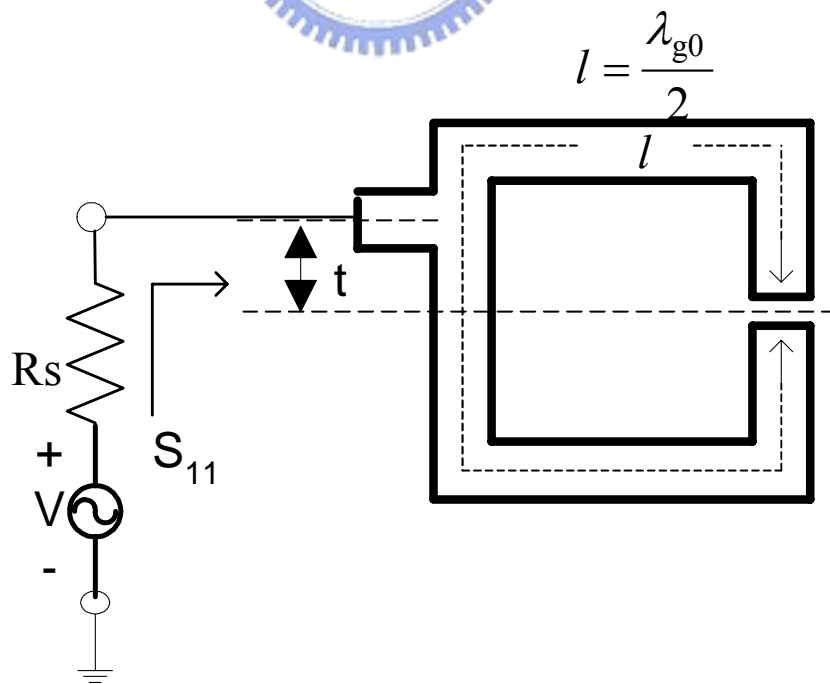
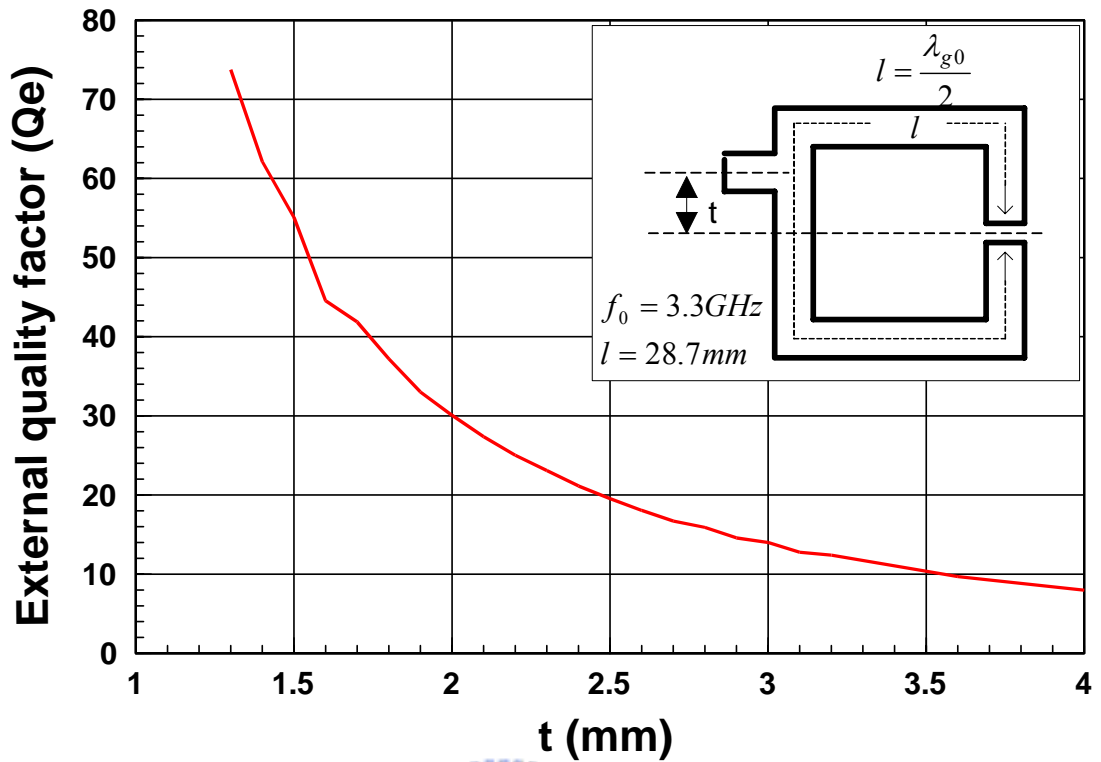
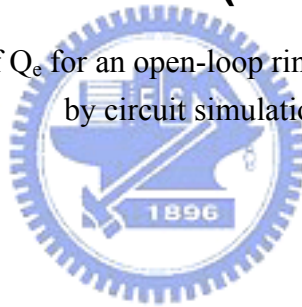


Figure 3.7 A half-wavelength open-loop ring resonator with a feed line



**Figure 3.8** Design curves of  $Q_e$  for an open-loop ring microstrip band-pass filter obtained by circuit simulation.



### 3.3 coupling coefficient design curves

In chapter 2, in order to realize the open loop ring band-pass filters, not only the introduced  $Q_e$  design curves, but also the coupling coefficient design curves are needed. In this section, we will introduce how to find out the coupling coefficient curves.

### 3.3.1 electric coupling and magnetic coupling structures

Figure 3.9 is typical coupling structures of coupled microstrip square open-loop resonators. These structures contain different orientations of a pair of identical square open-loop resonators being separated by a spacing  $S$  and an offset distance  $d$ .

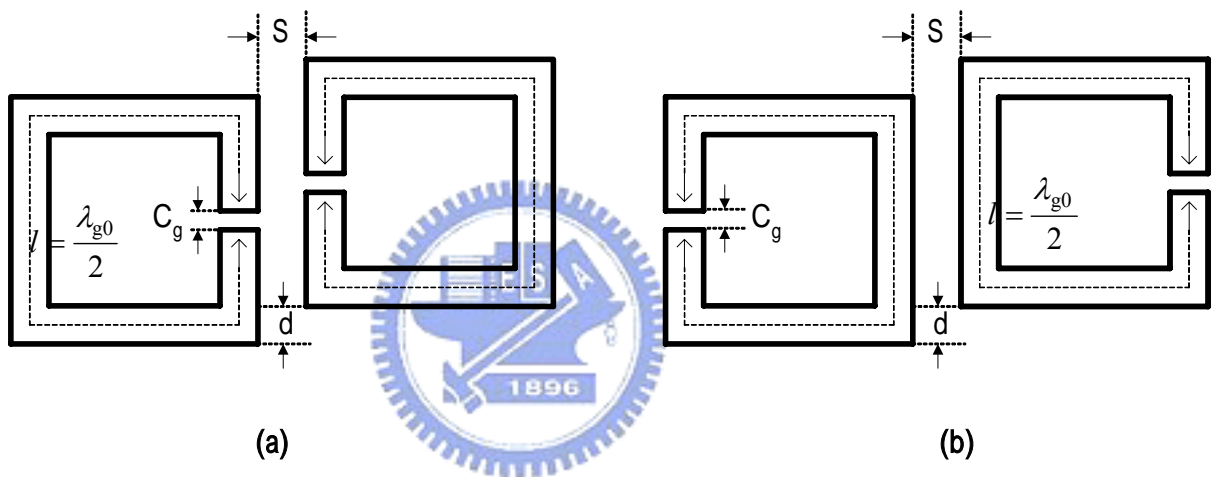


**Figure 3.9** Typical coupling structures of coupled microstrip square open-loop resonators  
(a) Electric coupling structure. (b) Magnetic coupling structure.

Because the open-loop resonators have the maximum electric field at the side with an open-gap and the maximum electric fringing field distribution there, the structure in the Figure 3.9 (a) is called the electric coupling structure. As shown in Figure 3.9 (b), we may conjecture that the coupling is mainly due to the magnetic field caused by the electric currents on the two parallel metal strips. Meanwhile, the faraway of the two open gaps may affect in considerably in this coupling procedure. Thus structure in the Figure 3.9 (b) is called the magnetic coupling structure.

### 3.3.2 electric coupling design curves

Figure 3.10 (a) is an equivalent lumped-element circuit of electric coupling structure for RF/microwave resonators in figure 3.9 (a), where  $C$  and  $L$  are the self capacitance and self inductance, so that  $(LC)^{-1/2}$  defines the angular resonant frequency of each uncoupled resonators.  $C_m$  represents the mutual capacitance. Because the structure under consideration is a distributed circuit, the lumped-element equivalent circuit is valid on a narrow-band, namely, near its resonance frequency. Now, we look into reference planes  $T_1-T'_1$  and  $T_2-T'_2$ , if a sinusoidal waveform is assumed, this circuit can be regarded as a two-port network and its voltage and current waves satisfy the equation given below:

$$I_1 = j\omega C V_1 - j\omega C_m V_2 \quad (3.17)$$

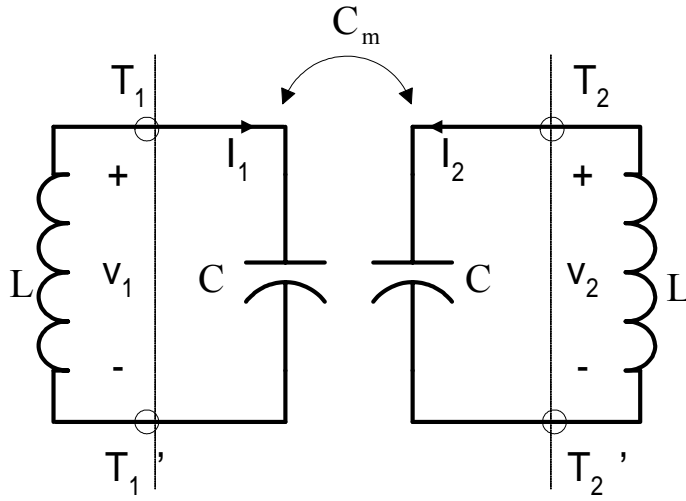
$$I_2 = j\omega C V_2 - j\omega C_m V_1 \quad (3.18)$$



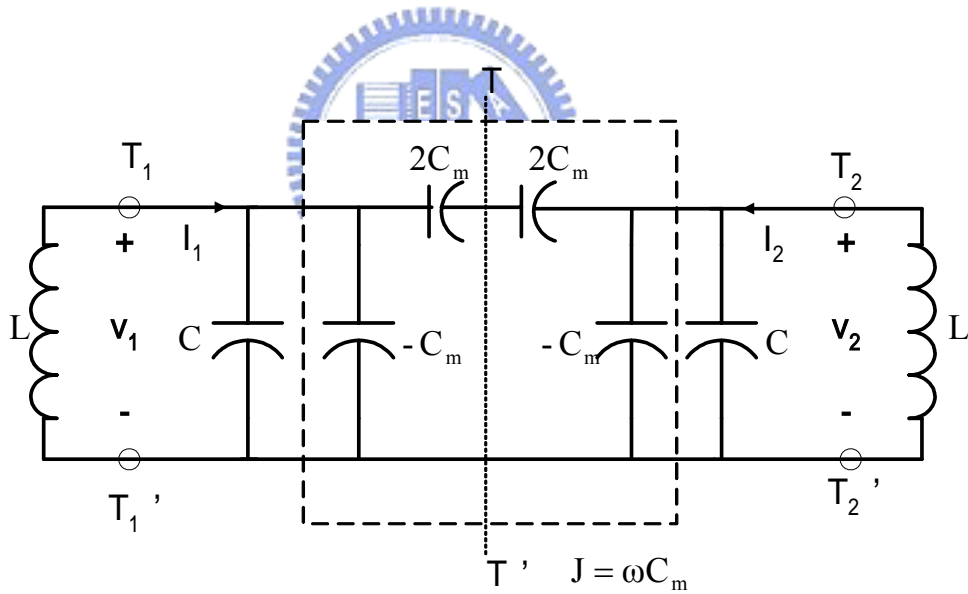
Form (3.17) and (3.18) the Y-parameters matrix can easily be found by definitions. It is

$$\begin{bmatrix} Y_{11} & Y_{12} \\ Y_{21} & Y_{22} \end{bmatrix} = \begin{bmatrix} j\omega C & -j\omega C_m \\ -j\omega C_m & j\omega C \end{bmatrix} \quad (3.19)$$

, and using the network theory [12] to the Figure 3.10 (b), we can find that the Y-parameter matrix looked from reference planes  $T_1-T'_1$  and  $T_2-T'_2$  in Figure 3.10 (b) is equivalent to equation (3.19), so an alternative form of the equivalent circuit in Figure 3.10(a) can be obtained and is shown in Figure 3.10(b). This circuit is more convenient to discuss the coupling coefficient of the electric coupling structures.



(a)



(b)

**Figure 3.10** (a) An equivalent lumped-element circuit of electric coupling structure (b) An alternative form of the equivalent circuit with an admittance inverter  $J = \omega C_m$

If we replace a short circuit (electric wall) in the symmetry plane T-T' in Figure 3.10 (b), the resultant circuit has a resonant frequency such as equation (3.20). This resonant frequency is

lower than that of an uncoupled single resonator. A physical explanation is that when the electric wall is inserted in the symmetrical plane of the coupled structure, the coupling and the resonant frequency becomes:

$$f_e = \frac{1}{2\pi\sqrt{L(C+C_m)}} \quad (3.20)$$

However, if we replace an open circuit (magnetic wall) in the symmetry plane T-T' in Figure 3.10 (b), the resultant circuit has a higher resonant frequency than that of without coupling

$$f_m = \frac{1}{2\pi\sqrt{L(C-C_m)}} \quad (3.21)$$

Equation (3.20) and (3.21) can be used to find the electric coupling coefficient  $k_E$ , it is

$$k_E = \frac{f_m^2 - f_e^2}{f_m^2 + f_e^2} = \frac{C_m}{C} \quad (3.22)$$

In the equation (3.21) we can find that  $k_E$  is identical to the definition of ratio of the coupled electric energy to the stored energy of uncoupled single resonator.

Now, we will induce how use equation (3.22) to find the coupling coefficients of the structure in Figure 3.9 (a). In Figure 3.9(a), if the coupled resonator circuits are over-coupled [1]; that is when the coupling coefficient is greater than the reciprocal of the quality factor of the resonator, the transmission coefficient  $S_{21}$  of the coupling structure can be presented in Figure 3.11. This Figure presents the two split resonant frequencies  $f_e$  and  $f_m$  at  $S=0.3\text{mm}$  or  $S=0.6\text{mm}$ . Substituting  $f_e$  and  $f_m$  into equation (3.22), the electric coupling coefficients can be found as shown in Figure 3.12. It is obtained by circuit simulation for the structure of Figure 3.9 (a) on the RO4003C substrate with  $f_0=3.3\text{GHz}$ , the relative dielectric constant  $\epsilon_r=3.38$ , thickness  $h=0.508\text{mm}$ , loss tangent  $\tan \delta = 0.0027$ , the gap  $g=0.5\text{mm}$  and the offset  $d=0$ .



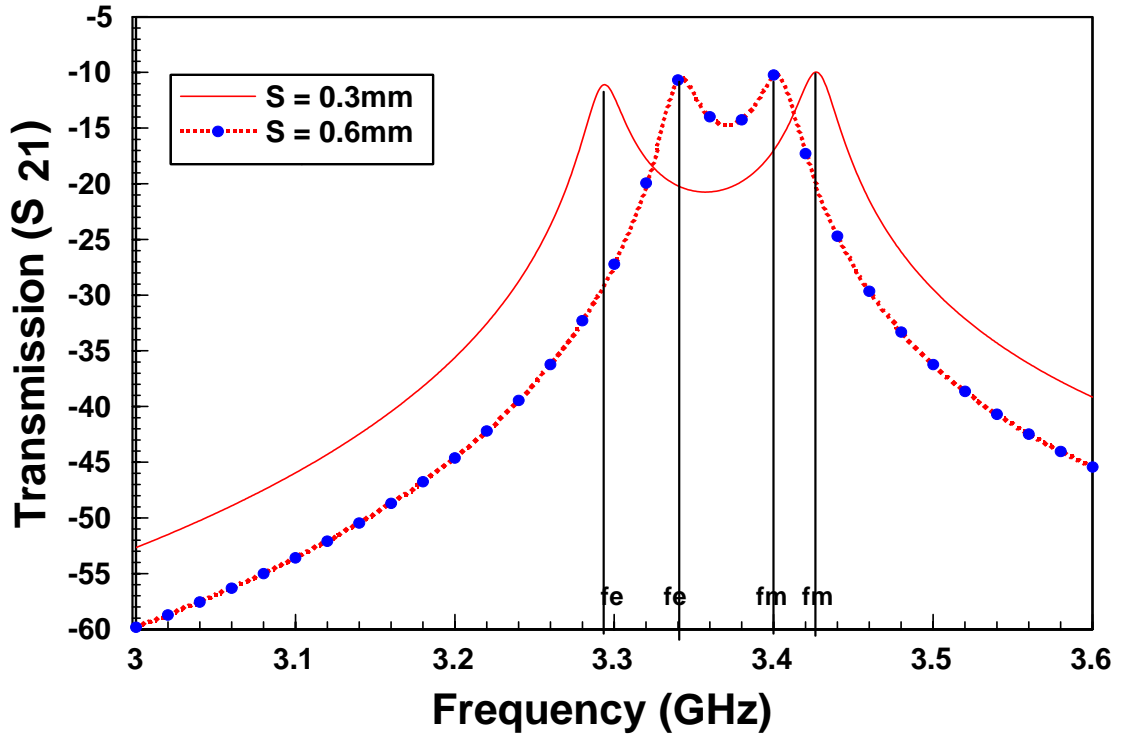


Figure 3.11 The  $S_{21}$  responses for the electric structure when the coupled resonator circuits are over-coupled

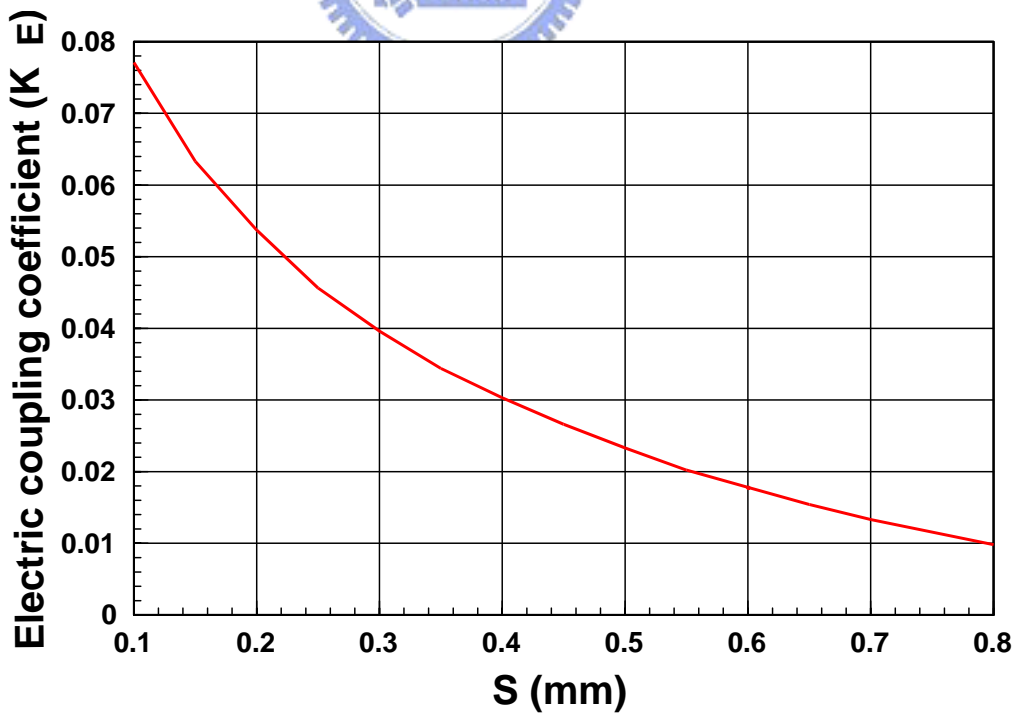


Figure 3.12 The coupling coefficient curve for the electric coupled resonator structure

### 3.3.3 magnetic coupling coefficient design curves

Similar to the electric structure, Figure 3.13 (a) is an equivalent lumped-element circuit of magnetic coupling structure for RF/microwave resonators, where C and L are the self capacitance and self inductance, so that  $(LC)^{-1/2}$  defines the angular resonant frequency of the uncoupled resonators, and  $L_m$  represents the mutual inductance. Now, we look into the reference planes  $T_1-T'_1$  and  $T_2-T'_2$ , if a sinusoidal waveform is assumed, a two-port network which may be described by equation (3.23) (3.24).

$$V_1 = j\omega LI_1 + j\omega L_m I_2 \quad (3.23)$$

$$V_2 = j\omega LI_2 + j\omega L_m I_1 \quad (3.24)$$

From (3.23) and (3.24) the Z-parameters matrix can easily be found by definitions. It is

$$\begin{bmatrix} Z_{11} & Z_{12} \\ Z_{21} & Z_{22} \end{bmatrix} = \begin{bmatrix} j\omega L & j\omega L_m \\ j\omega L_m & j\omega L \end{bmatrix} \quad (3.25)$$

Similarly, using the network theory [12], Figure 3.13 (b) is an alternative form of equivalent circuits having the same network parameters as those of Figure 3.13 (a). It can be shown that the magnetic coupling between the two resonant loops is represented by an impedance inverter  $K=\omega L_m$ . If the symmetry plane T-T' in Figure 3.13 (b) is replaced by a short circuit (or an electric wall), the circuit has a resonant frequency such as equation (3.26).

$$f_e = \frac{1}{2\pi\sqrt{(L - L_m)C}} \quad (3.26)$$

From equation (3.26), we could know that the resonant frequency is higher than that of an uncoupled resonator. If the plane T-T' in Figure 3.13 (b) is replaced by an open circuit (or magnetic wall), it has a resonant frequency such as equation (3.27).

$$f_m = \frac{1}{2\pi\sqrt{(L + L_m)C}} \quad (3.27)$$

and that the resonant frequency shifts toward lower frequency.

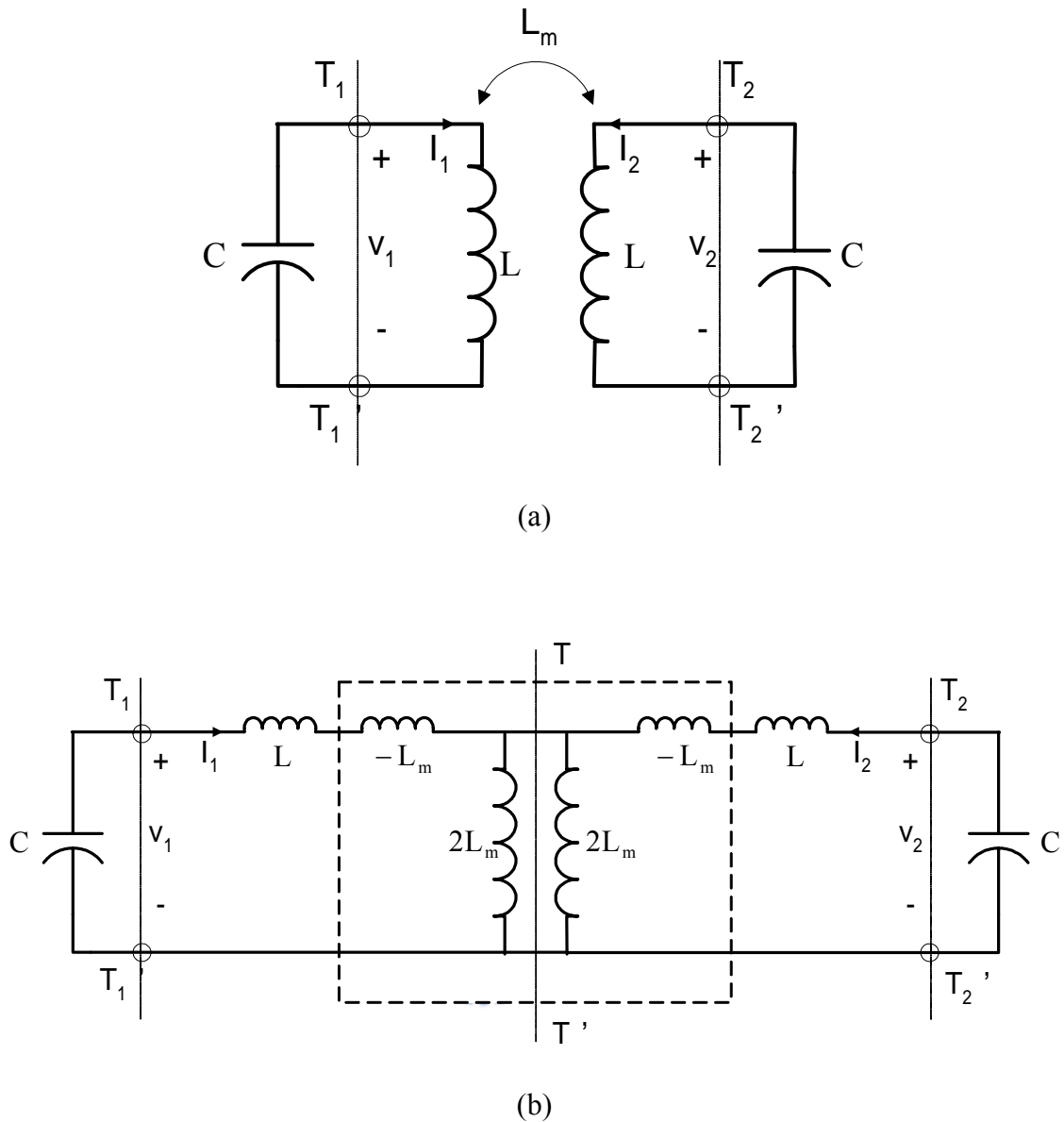


**Figure 3.13** (a) An equivalent lumped-element circuit of magnetic coupling structure (b) An alternative form of the equivalent circuit with an impedance inverter  $K = \omega L_m$

It is worthy to note that the short circuit bisection (SCB) will increase its resonant frequency, however, the situation of open circuit bisection (OCB) contrasts. This is because that the OCB has the symmetric field distribution and thus the same direction of current flow cause positive mutual inductance  $L_m$ , and the total inductance increases accordingly. On the contrary, the asymmetric current distribution with the SCB case results in negative mutual inductance and thus it decrease the total inductance.

Similarly, equation (3.26) (3.27) can be used to determine the magnetic coupling coefficient  $K_m$ . it is

$$K_m = \frac{f_e^2 - f_m^2}{f_e^2 + f_m^2} = \frac{L_m}{L} \quad (3.28)$$

In this equation we can find  $k_m$  is identical with the definition that is the ratio of the coupled magnetic energy to the stored energy of uncoupled single resonator. Similarly, in Figure 3.9(b) if the coupled resonator circuits are over-coupled, the transmission coefficient  $S_{21}$  of the coupling structure can be presented in Figure 3.14. This Figure presents the two split resonant frequencies  $f_e$  and  $f_m$ . Substituting  $f_e$  and  $f_m$  on equation (3.28), the magnetic coupling coefficients can be found. Using the method, the magnetic coupling design curves can be found such as Figure 3.15. It is obtained by the circuit simulation on the RO4003C substrate with  $f_0=3.3\text{GHz}$ , the relative dielectric constant  $\epsilon_r=3.38$ , thickness  $h=0.508\text{mm}$ , loss tangent  $\tan \delta = 0.0027$ , the gap  $g=0.5\text{mm}$  and the offset  $d=0$ .

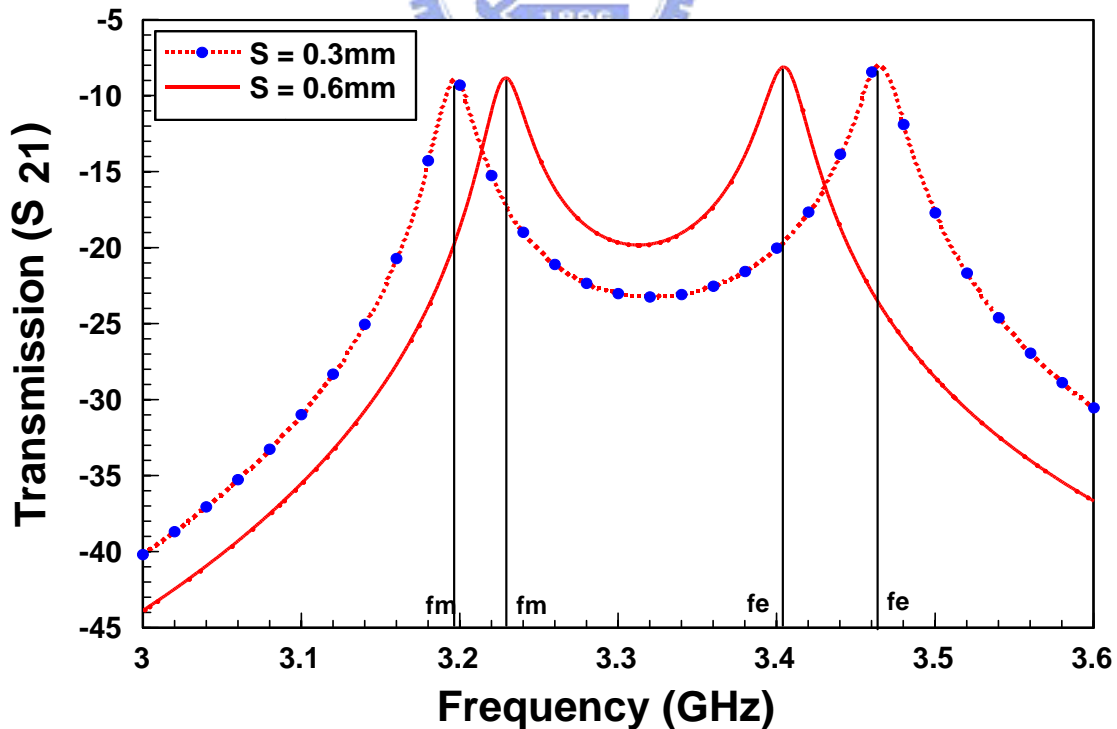


**Figure 3.14** The  $S_{21}$  responses for the magnetic coupling structure when the coupled resonator circuits are over-coupled

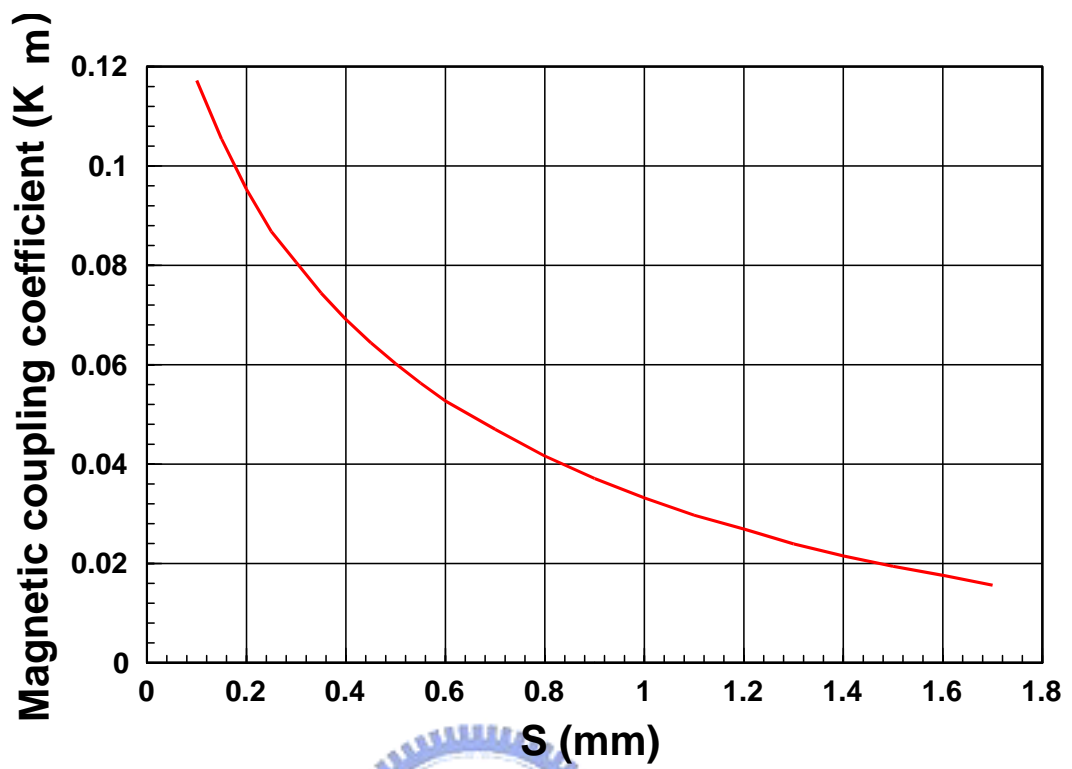
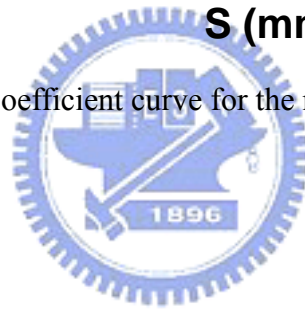


Figure 3.15 The coupling coefficient curve for the magnetic coupled resonator structure

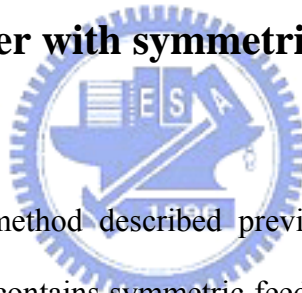


# Chapter 4

## Practical realization of the band-pass filter for microstrip

In this chapter we will carry out both circuit simulation and experimental studies for the band-pass filters by using microstrip-line. Beside the design of asymmetric feed lines was to employed increase the selectivity of the filters [5].

### 4.1 The Band-pass filter with symmetric feed lines



Now, we will use the method described previously to design an opened-loop ring band-pass filter. The structure contains symmetric feed lines shown in Figure 4.1. The center frequency  $f_0 = 3.3\text{GHz}$  ( $\lambda_{g0}/2=28.7\text{mm}$ ), frequency bandwidth  $\text{BW}=150\text{MHz}$  ( $\text{FBW}=0.045$ ), open gap  $g=0.5\text{mm}$ , order  $n=2$ , using RO4003C substrate, relative dielectric constant  $\epsilon_r=3.38$ , thickness  $h=0.508\text{mm}$ , loss tangent  $\tan \delta = 0.0027$ . By the appendix A, when the  $n=2$ , the required  $g_0=1$ ,  $g_1=g_2=1.414$ ,  $g_3=1$ . Substituting they into (2.24) (2.25) (2.26), the external quality factor can be found as  $Q_{e1} = Q_{e2}=31.4$  and the electric coupling coefficient is  $K_{12}=0.0318$ . If the  $Q_{e1}$ ,  $Q_{e2}$  and  $K_{12}$  are substituted into the  $Q_e$  design curve in the Figure 3.8 and  $K_E$  design curve in Figure 3.12 respectively, the tapping position and the required gap can be found as  $t=2\text{mm}$  and  $S=0.5\text{mm}$ . Figure 4.2 depicts the calculated and measured insertion loss, while those of return loss are shown in Figure4.3. This filter has a measured insertion loss, 1.67dB, and return loss, 14.5dB, at the center frequency 3.3GHz.

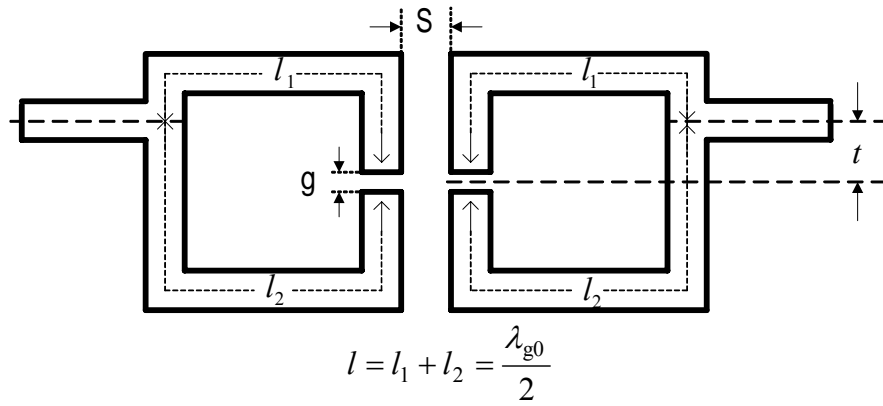


Figure 4.1 The open-loop ring band-pass filter with the symmetric feed lines

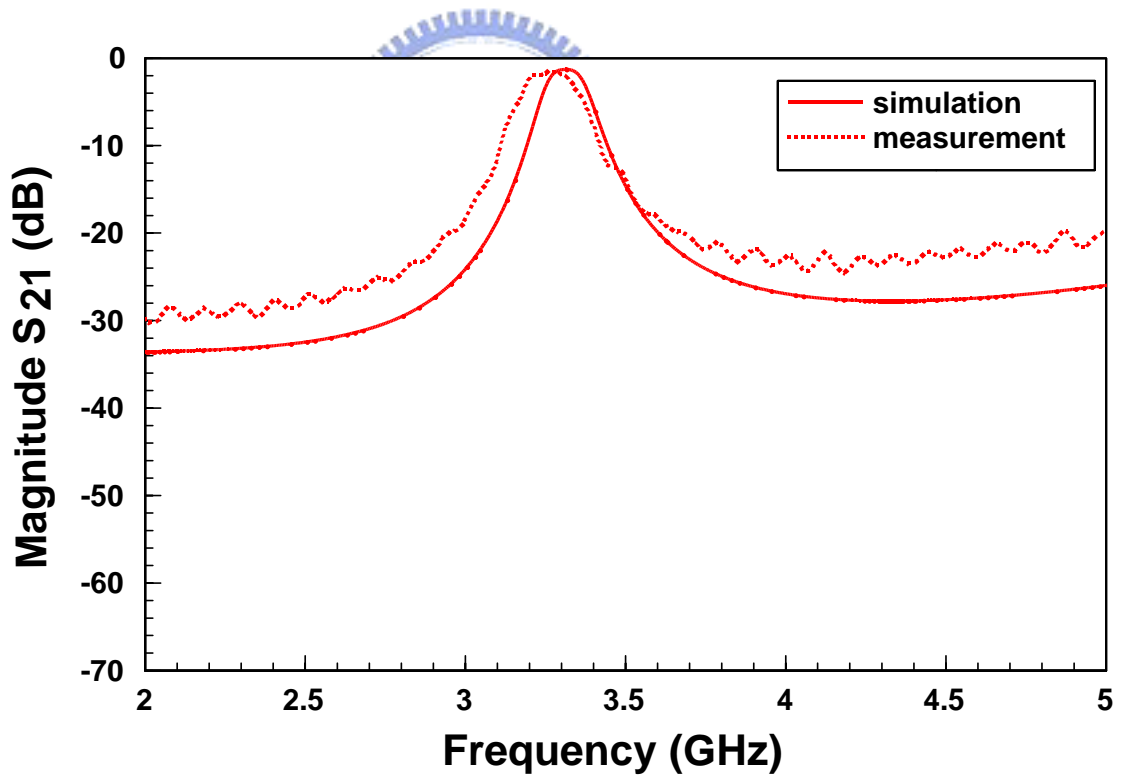
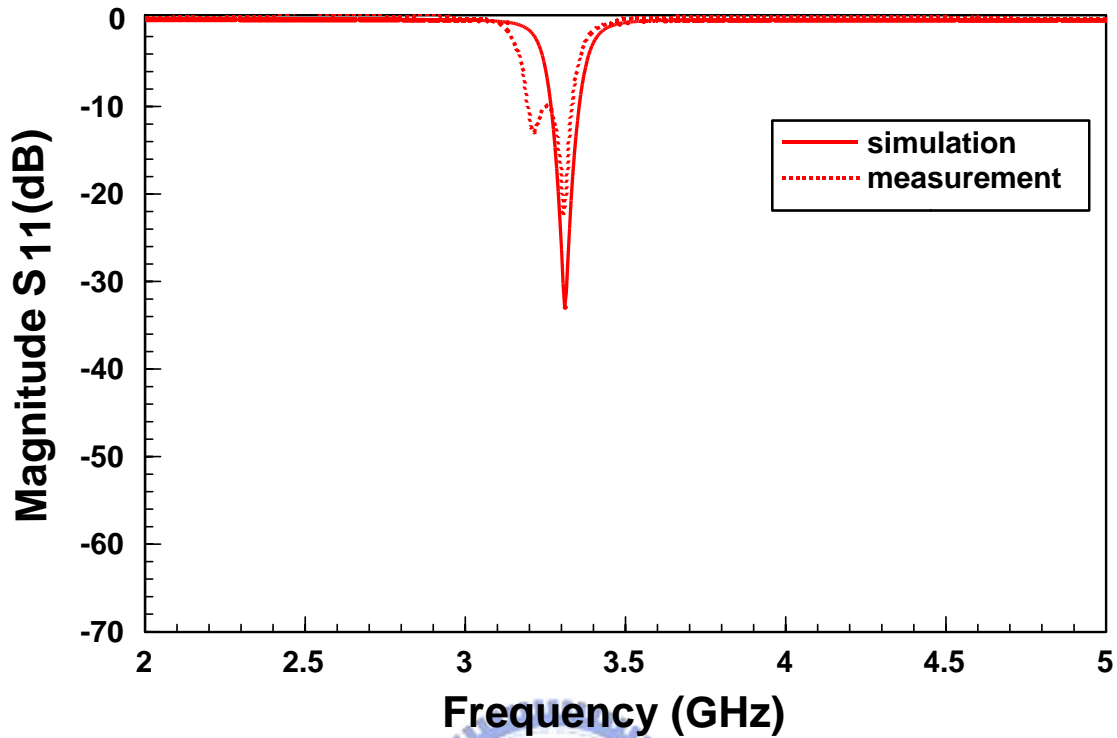


Figure 4.2 The  $S_{21}$  of simulation and measurement for the open-loop ring band-pass filter with the symmetric feed lines



**Figure 4.3** The  $S_{11}$  of simulation and measurement for the open-loop ring band-pass filter with the symmetric feed lines

## 4.2 The Band-pass filter with asymmetric feed lines

In this section we will introduce a method using asymmetric feed lines, which possesses two transmission zeros. This method has an advantage which can increase the selectivity of the filter on that the filter, however, the size is not increased. Figure 4.4 is a band-pass filter using two hairpin resonators with asymmetric feed lines, where the length of resonator  $l = l_1 + l_2 = \lambda_{g0}/2$  and the coupling between the two open ends of the resonators is simply expressed by the gap capacitance.



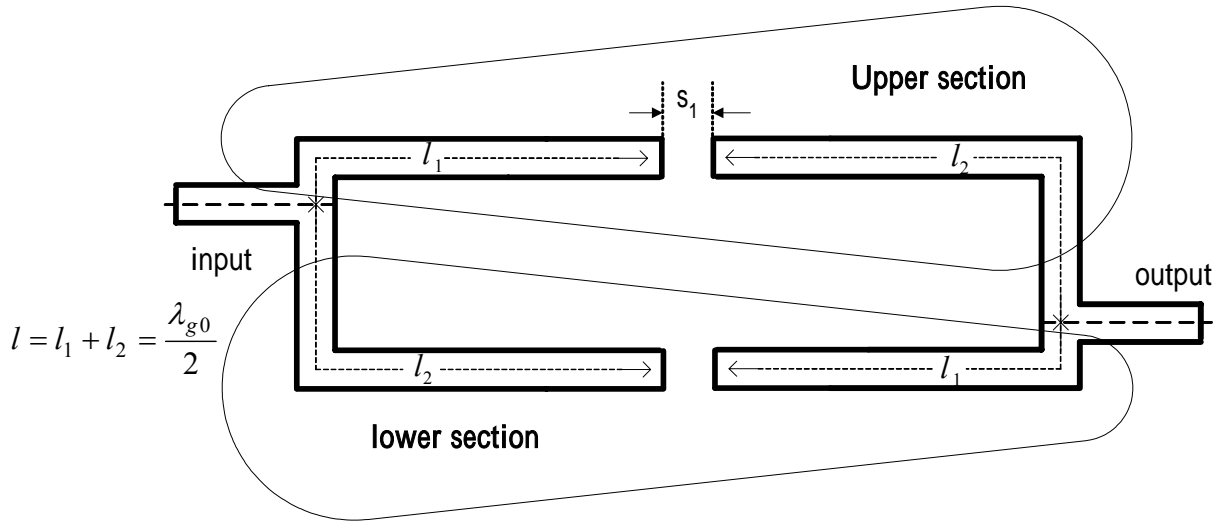


**Figure 4.4** The filter using two hairpin resonators with asymmetric tapping feed lines

From this configuration, the circuit represents a shunt circuit, which consists of upper and lower sections. The ABCD matrices for the upper and lower section circuit are

$$\begin{pmatrix} A & B \\ C & D \end{pmatrix}^{upper} = M_1 M_2 M_3 \quad (4.1)$$

$$\begin{pmatrix} A & B \\ C & D \end{pmatrix}^{lower} = M_3 M_2 M_1 \quad (4.2)$$

If the circuit is lossless, the  $M_1, M_2, M_3$  in the equation (4.1) (4.2) are the ABCD matrices of  $l_1, l_2$  and  $C_s$  respectively such as

$$M_1 = \begin{pmatrix} \cos(\beta l_1) & jZ_0 \sin(\beta l_1) \\ j\frac{1}{Z_0} \sin(\beta l_1) & \cos(\beta l_1) \end{pmatrix} \quad (4.3)$$

$$M_2 = \begin{pmatrix} 1 & Z_k \\ 0 & 1 \end{pmatrix} \quad (4.4)$$

$$M_3 = \begin{pmatrix} \cos(\beta l_2) & jZ_0 \sin(\beta l_2) \\ j\frac{1}{Z_0} \sin(\beta l_2) & \cos(\beta l_2) \end{pmatrix} \quad (4.5)$$

, where  $\beta$  is the propagation constant,  $Z_k = 1/(j\omega C_s)$  is the impedance of the gap capacitance  $C_s$ ,  $Z_0$  is the characteristic impedance of the resonator. By the transformation in

the ABCD parameters to the Y parameter, equation (4.1) (4.2) can be transformed into the Y parameters  $Y_{upper}$  and  $Y_{lower}$ , respectively. The total Y-parameters of this filter circuit can be obtained by adding  $Y_{upper}$  and  $Y_{lower}$ , and the  $S_{21}$  of this filter can be obtained by transforming Y matrix to S matrix, which is given as:

$$S_{21} = \frac{\frac{4}{Z_0}(jZ_0 \sin(\beta l) + Z_k \cos(\beta l_1) \cos(\beta l_2))}{\left(2 \cos(\beta l) - \frac{jZ_k \sin(\beta l)}{Z_0} + \frac{Z_0 \sin(\beta l) + jZ_k \cos(\beta l_1) \cos(\beta l_2)}{Z_0}\right)^2 - 4} \quad (4.6)$$

the transmission zeros can be found by letting  $S_{21}=0$ , namely

$$jZ_0 \sin(\beta l) + Z_k \cos(\beta l_1) \cos(\beta l_2) = 0 \quad (4.7)$$

for a small  $C_S$  ( $Z_k \gg Z_0$ ), (4.7) can be approximated as

$$\cos(\beta l_1) \cos(\beta l_2) \approx 0 \quad (4.8)$$

substituting  $\beta = 2\pi f \sqrt{\epsilon_{eff}} / c$  into (4.8), the transmission zeros corresponding to the tapping positions are

$$f_1 = \frac{mc}{4l_1 \sqrt{\epsilon_{eff}}} \quad (4.9.a)$$

$$f_2 = \frac{mc}{4l_2 \sqrt{\epsilon_{eff}}} \quad (4.9.b)$$

, where  $\epsilon_{eff}$  is the effective dielectric constant, m is the mode number and c is the speed of light in free space. Furthermore, Figure 4.5 is an open-loop ring band-pass filter with asymmetric feed lines. This Filter is similar to Figure 4.4, except for the two addition 45° chamfered bends and the coupling gap g between the two open ends of the ring. In [5], the measurement data have verified the two transmission zeros by using (4.9.a) (4.9.b). Here, we also design a filter show in Figure 4.5 to identify equation (4.9). Because this filter has the same structure configuration and design parameters ( $f_0=3.3\text{GHz}$ ,  $\text{FBW}=0.045$ ) as that filter in Figure 4.1, where  $l=28.7\text{mm}$ ,  $t=1.95\text{mm}$ ,  $S=0.5\text{mm}$ ,  $l_1=12.4\text{mm}$  and  $l_2=16.3\text{mm}$ . The measured and simulated results of the filter are shown in Figure 4.6 and Figure 4.7. This Filter

has a measured insertion loss of 1.67 dB and return loss 14.5 dB at center frequency 3.3GHz. The two transmission zeros are  $f_1=3.8125\text{GHz}$  ,  $f_2=2.92\text{GHz}$ , respectively, which can be observed in Figure 4.6. They are very close to the values  $f_1=3.72\text{GHz}$  and  $f_2=2.83\text{GHz}$  obtained by equation (4.9). In order to refer easily, we put them together and show in Figure 4.8, and we can distinctly find that the transmission zeros are caused by asymmetric feed lines indeed increase the selectivity of the filter.

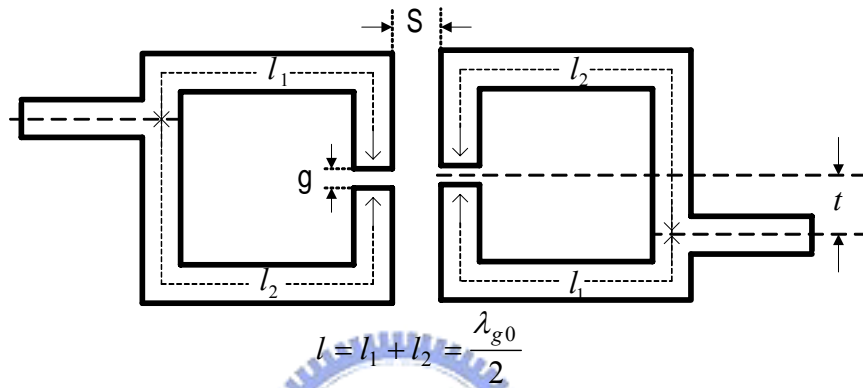


Figure 4.5 The open-loop ring band-pass filter with the asymmetric feed lines

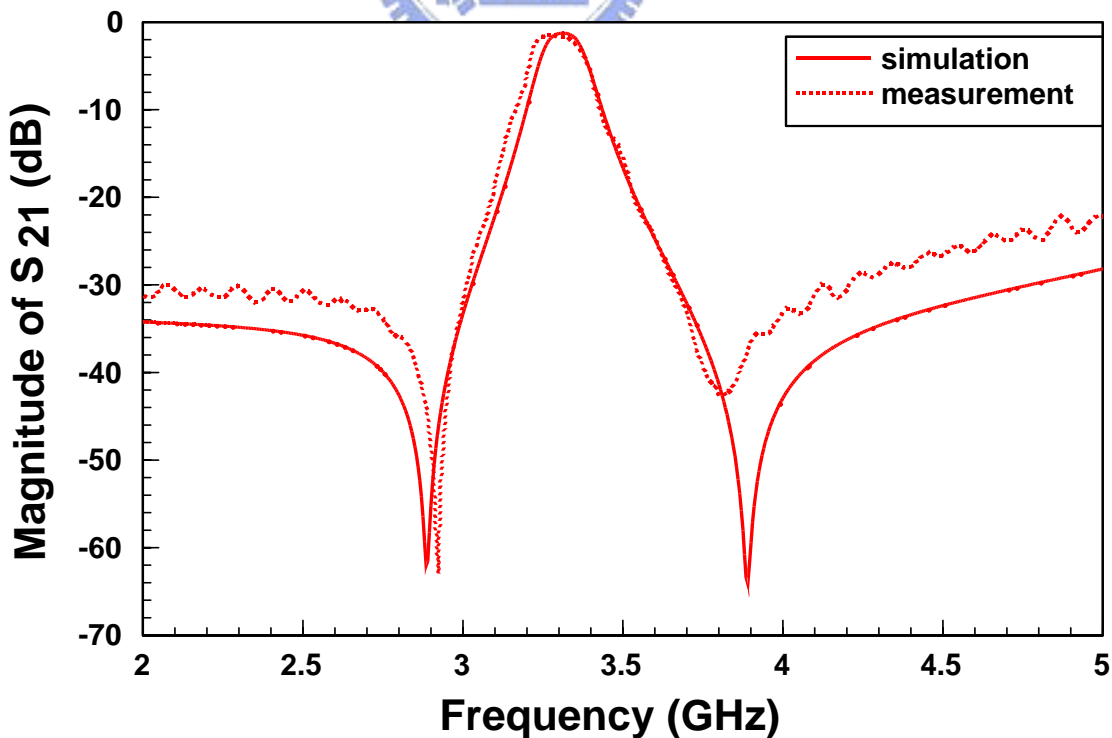


Figure 4.6 The  $S_{21}$  of simulation and measurement for the open-loop ring band-pass filter with the asymmetric feed lines

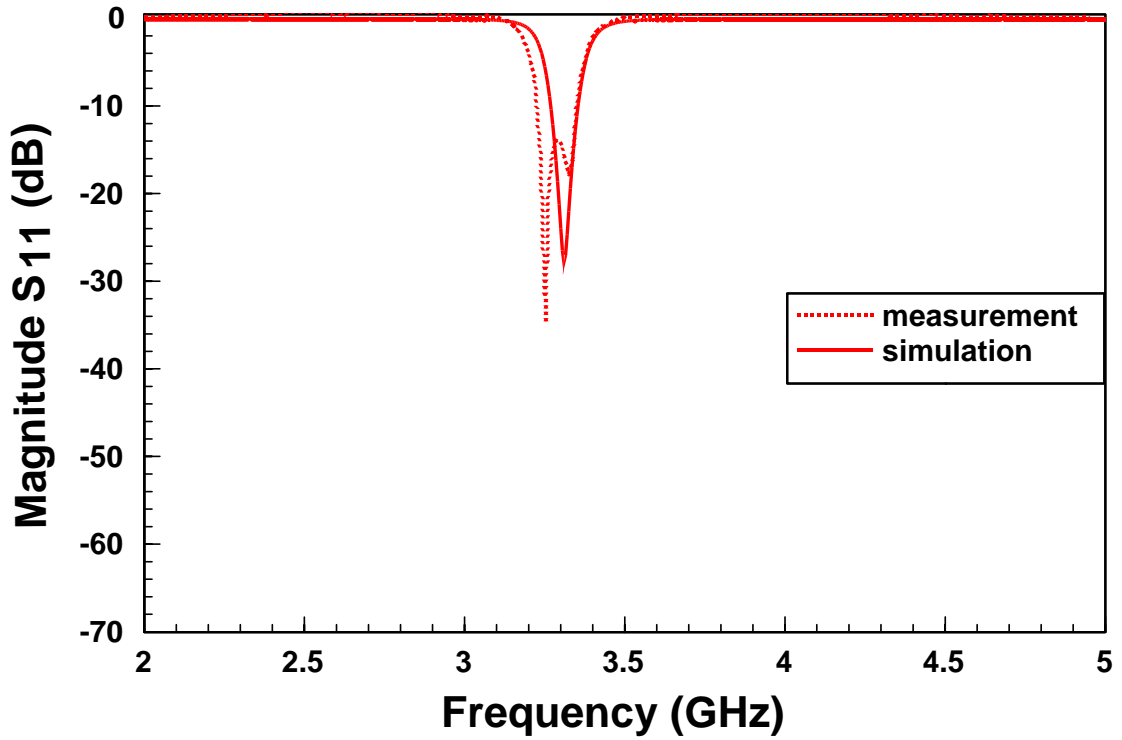


Figure 4.7 The  $S_{11}$  of simulation and measurement for the open-loop ring band-pass filter with the asymmetric feed lines

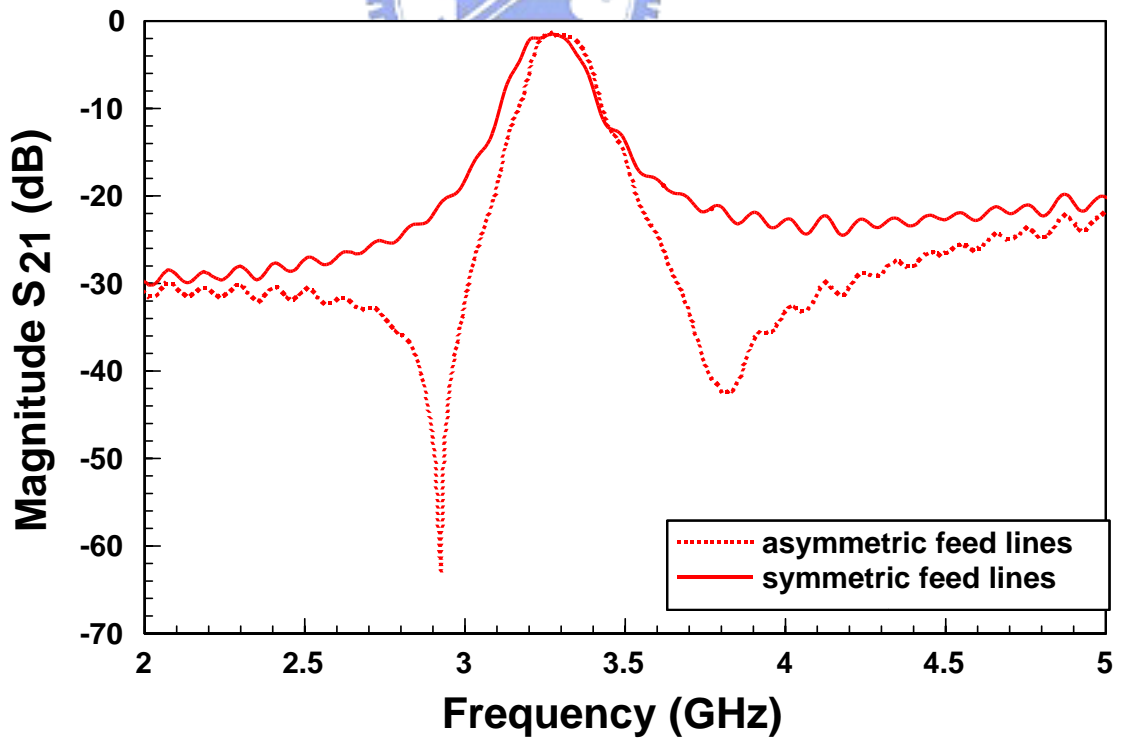
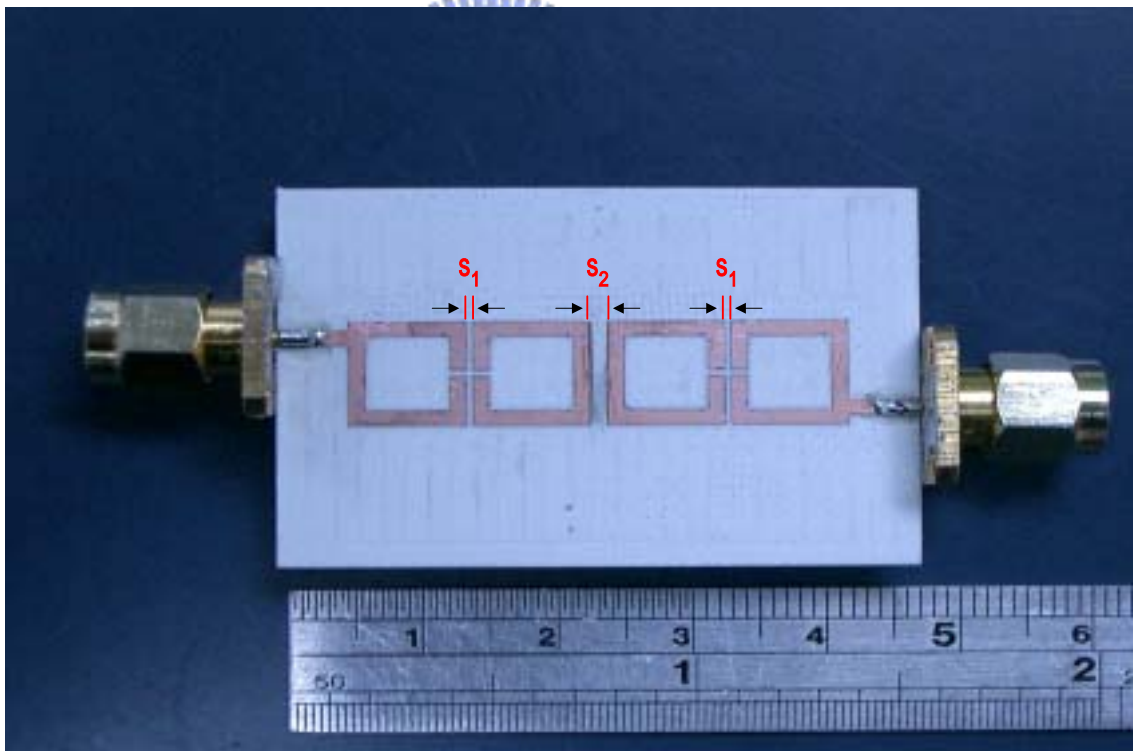
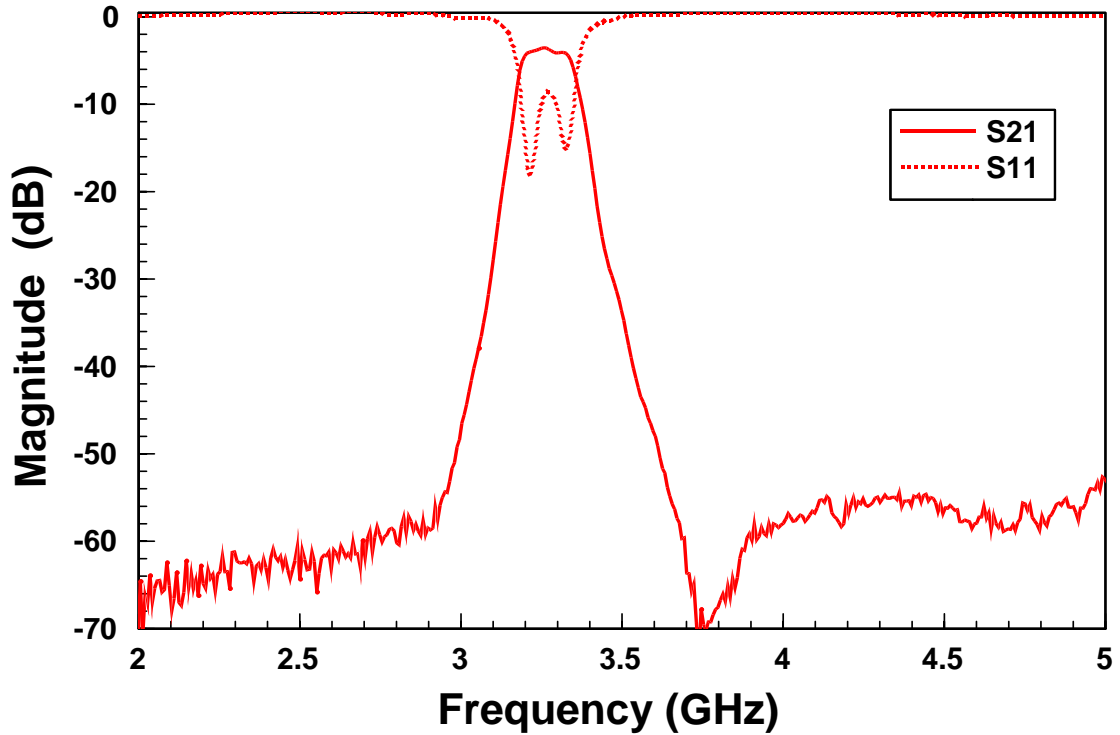


Figure 4.8 The  $S_{21}$  of measurement for the open-loop ring band-pass filter with the symmetric and asymmetric feed lines

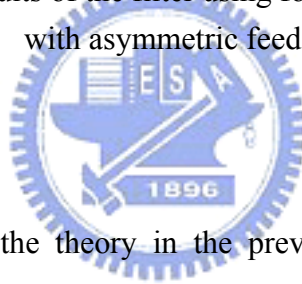
To further increase the selectivity of the filter, we could cascade two sections of the original ones to achieve the purpose. In the following example, we will implement this idea by using four open-loop rings. The design criteria of the circuit is similar to the previous one, namely  $f_0=3.3\text{GHz}$  and  $\text{FBW}=0.045$ . The needed  $g_0=1=g_5$ ,  $g_1=0.7645$ ,  $g_2=1.8478=g_3$  and  $g_4=0.7645$  can be found in Appendix A with  $n=4$ . Substituting them into (2.24)(2.25)(2.26), The external quality factor  $Q_{e1}=Q_{e4}=31.4$ , electric coupling coefficients  $K_{12}=K_{34}=0.0378$ , magnetic coupling coefficients  $K_{23}=0.0244$ , and by  $Q_e$ ,  $K_E$ ,  $K_m$  design curves, the needed feed line position  $t=2.1\text{mm}$  and the required gap  $S_1=0.45\text{mm}$ ,  $S_2=1.2\text{mm}$ . Figure 4.10 presents the measured results. It is obviously to find that the selectivity of the filter is increased.



**Figure 4.9** The layout of the filter using four cascaded open-loop ring resonators with the asymmetric feed lines.



**Figure 4.10** The measured results of the filter using four cascaded open-loop ring resonators with asymmetric feed lines.



In this chapter, we use the theory in the previous chapter to design, fabricate and measure the performance of the filter shown Figure 4.1. In addition, we have also verified that the asymmetric feed lines can drastically enhance the selectivity by introducing two transmission zeros, however, maintain its size. Furthermore, the asymmetric feed lines can be used with higher  $n$  filter such as Figure 4.9, and it can increase the selectivity of filter more.

# Chapter 5

## The design method and realization of the tunable band-pass Filters

In this chapter we will propose a new method that can switch the resonant frequency of the open loop ring resonator. Beside, we also designed and fabricated some tunable band-pass filters. The results from simulation and measurement will also be presented in this chapter.

### 5.1 The mechanism of frequency tuning

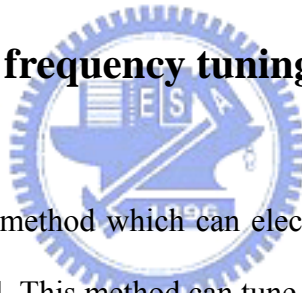


Figure 5.1 is a conventional method which can electrically tune the resonant frequency of the open loop ring resonator [8]. This method can tune the resonant frequency of the resonator by the tunable capacitance  $C_T$  of the varactor, and the  $C_T$  can be tune by the reverse bias. When the capacitance is increased, the resonant frequency of the resonator will be decreased. In order to have the frequency capability tuning, five devices are needed shown in Figure 5.1, where two capacitors  $C$  are the DC choke, two inductors  $L$  are the RF choke and one varactor serves as a variable capacitor. This method is simply and conveniently, but its frequency range of tuning is not considerable.

In this section we will propose a new method to switch the resonant frequency of the open loop ring resonator. Figure 5.2 (a) is an equivalent circuit [15] of a varactor connecting to ground. where  $L_{via}$  is the equivalent inductance of the via hole ground, the parameter  $R_s$ ,  $C_p$ ,  $L_s$ ,  $L_p$ , are the parasitic resistor, capacitance and inductance caused by the varactor package, and

$C_T$  is variable capacitance that can be varied by the reverse bias. Figure 5.2(b) is the equivalent circuit that neglects the  $R_s$  and  $C_p$ , where  $L_T$  is the sum of the  $L_s$ ,  $L_p$  and  $L_{via}$ , namely,

$$L_T = L_s + L_p + L_{via} .$$

Now, we will apply the varactor equivalent circuit in Figure 5-2 (b) to Figure 5.3. Figure 5.3 is the new design which can tune the resonant frequency of the open loop ring resonator. This circuit not only has a wider frequency tuning range, but also has a smaller circuit size and fewer devices needed. Only four devices are used in this circuit, a capacitance  $C$  is a DC choke, an inductance  $L$  is an RF choke, and two varactors.

When  $1/\omega C_T > \omega L_T$  in the structure in Figure 5.3, the  $X$  is a negative number and the resonant frequency of this structure is smaller than that without the varactors. On the other hand, when  $1/\omega C_T < \omega L_T$ , the  $X$  is a positive number and the resonant frequency of this structure is greater than that without the varactors. Once the response curves for  $C_T$  and  $X$  against frequency are plotted, the tunable band-pass filters using this structure can be designed.

Before designing the tunable band-pass filter, we have to find the  $L_T$  in Figure 5.4. The  $L_T$  method for finding is shown in Figure 5.4, where  $C$  and  $L_T$  form a series LC resonator. The  $S_{21}$  of this circuit is zero when this series resonator is at the resonant frequency, and the  $L_T$  can be obtained as follows:

$$f_0 = 1/2\pi\sqrt{L_T C} \tag{5.1}$$



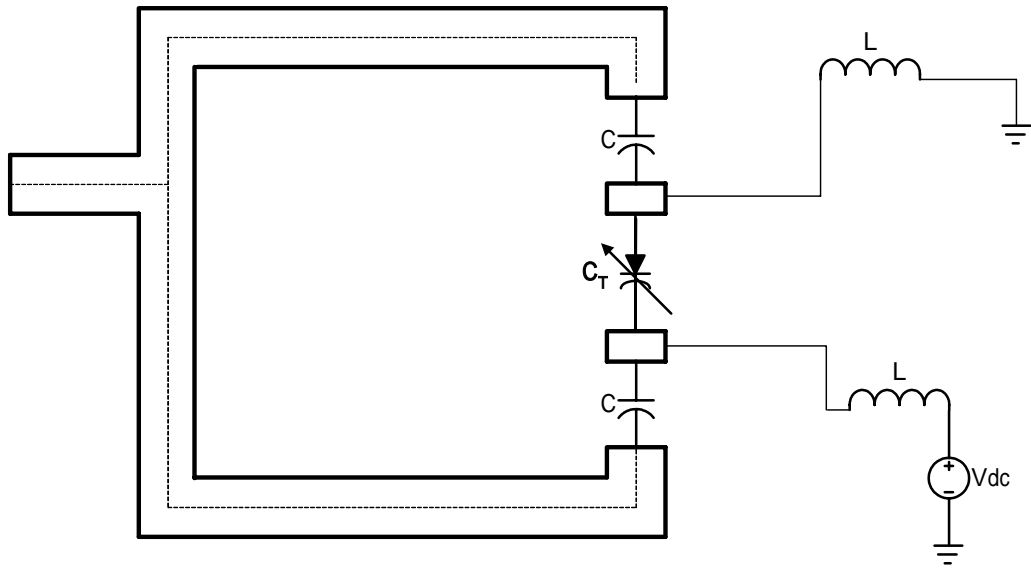


**Figure 5.1** The conventional structure for the electrically tunable frequency resonator

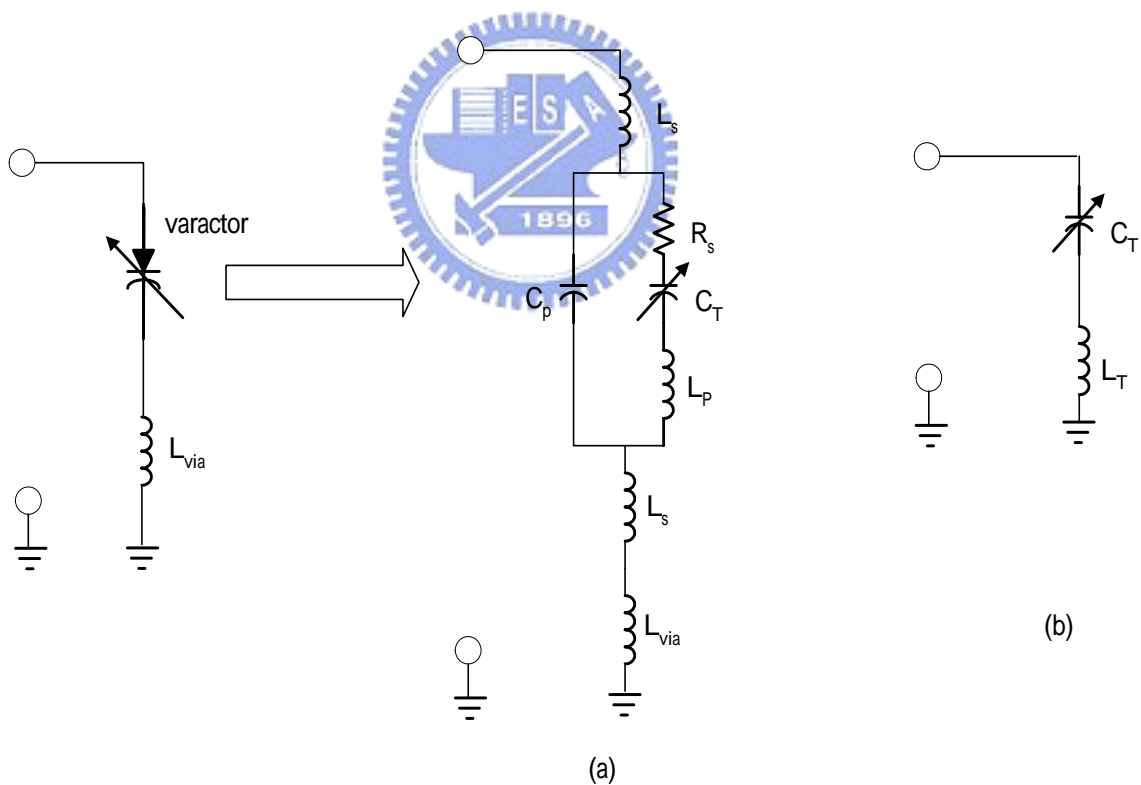


**Figure 5.2** The equivalent circuit for the varactor connect the via hole ground (a) considering the parasitic effects of the package (b) neglecting the parameter  $C_p$  and  $R_s$

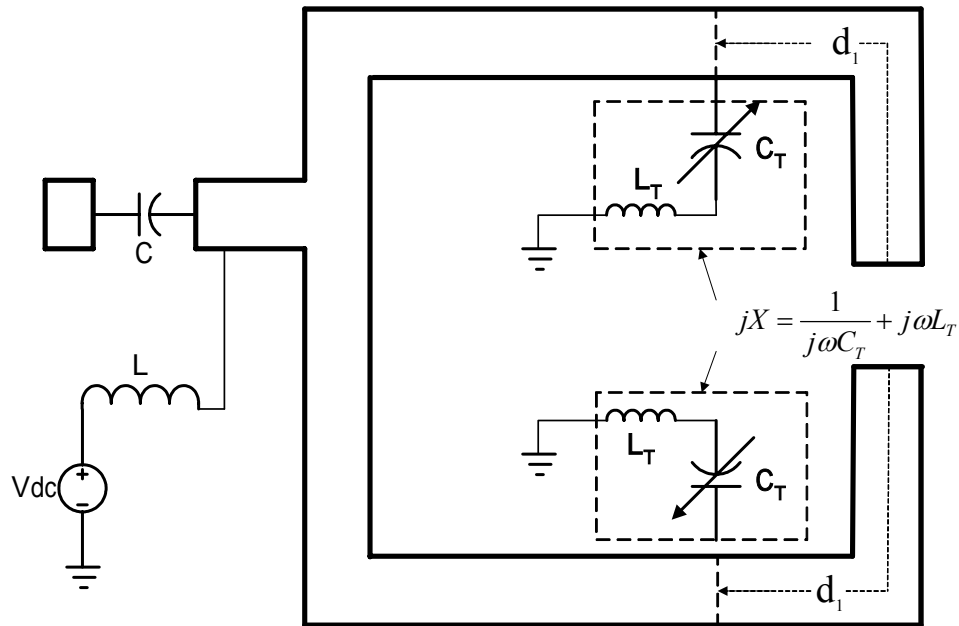


**Figure 5.3** The new structure for the electrically tunable frequency resonator

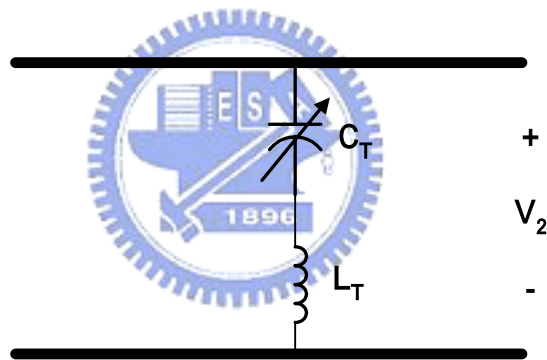


**Figure 5.4** The measurement circuit for  $L_T$

## 5.2 The tunable band-pass filter using capacitance reactance X

In section 5-1 we have known that if we could have the response curves for the resonant frequency versus the reactance, the tunable filter can be realized in practice. In this section we will use this new method to design a tunable band-pass filter using capacitance reactance X. In the design we use the substrate (RO4003C), the B-C electrodes of transistor NEC (2SC3356) are taken as anode and cathode of the varactor, the resonant frequency of the ring

resonator without varactor is 2 GHz ( $\lambda_0/2=47.6\text{mm}$ ), BW=50MHz,  $t=2.5\text{mm}$ ,  $S=0.7\text{mm}$ ,  $g=0.5\text{mm}$  and the varactor tapping position  $d_1=11.65\text{mm}$ . We find the  $L_T$  by the circuit Figure 5.4 circuit first. By the measured  $S_{21}$  of Figure 5.1, when  $C=1.4\text{ pF}$  (reverse bias  $V_R=30\text{V}$ ), the series LC resonant frequency is 5.48GHz and, by equation (5.1) we can find the  $L_T=2.2\text{nH}$ . Because the capacitance on the varactor was varied from 0.38 to 1.4 pF ( $V_R$  was varied from 30 to 0 V), the  $X$  was varied from -181.76 to -29.19 . Figure 5.5 is the variation of capacitance (reactance) against resonant frequency when the varactor is tapped at  $d_1=11.65\text{mm}$ . The curves present that the resonant frequency  $f_0$  is increased by decreased  $C_T$  ( $f_0$  is increase by decreasing  $X$ ). Using these curves, we design a tunable band-pass filter such as Figure 5.6. Figure 5.7 is the layout of this filter. The center frequency can be tuned form 1.86 to 1.5GHz. The insertion loss obtained from simulation and measurement are presented in Figure 5.8 and Figure 5.9 respectively.

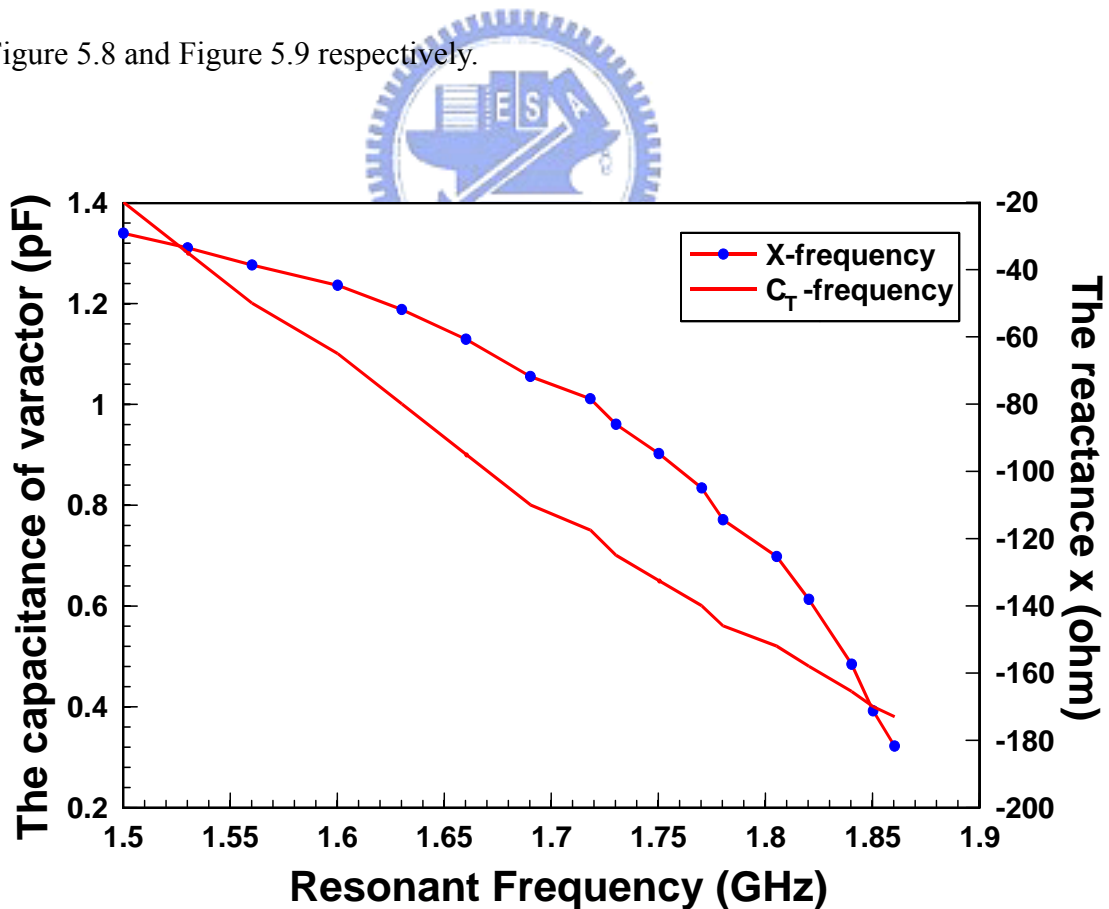
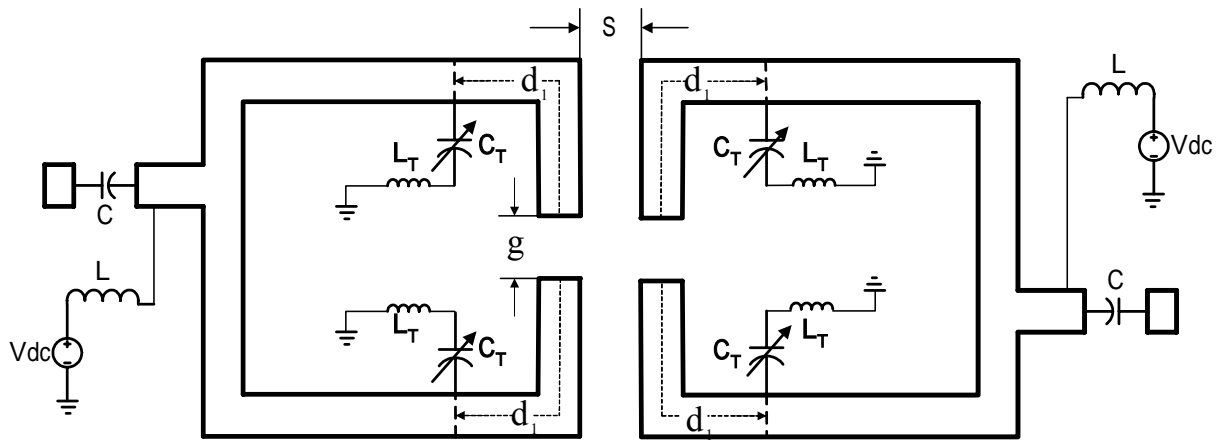
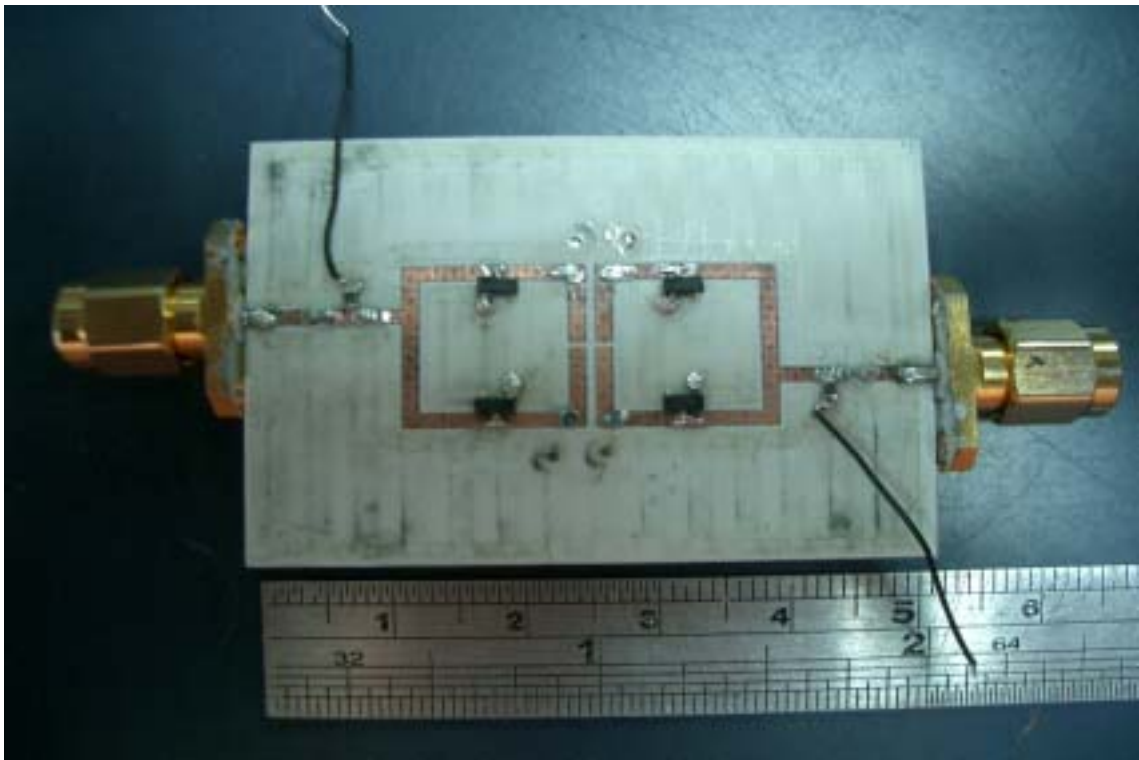


Figure 5.5 The simulated responses for  $C_T$  and  $X$  against  $f_0$



**Figure 5.6** The new tunable band-pass filter circuit



**Figure 5.7** The layout of the new tunable band-pass filter

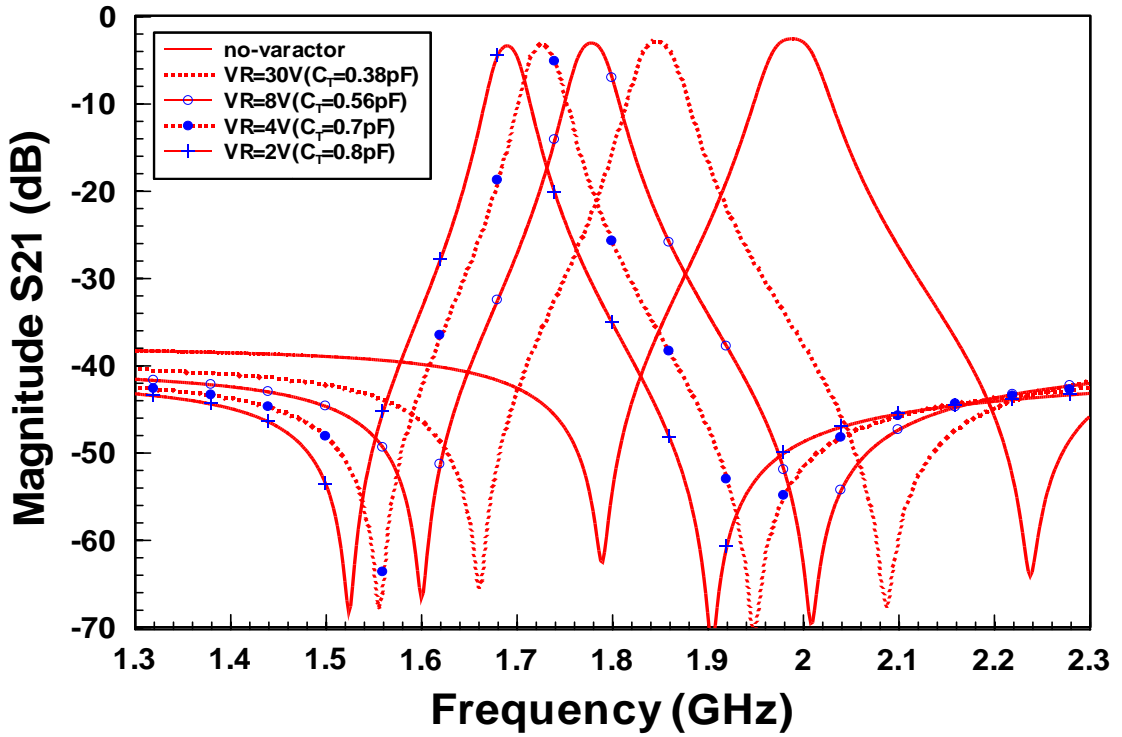


Figure 5.8 The simulation of the tunable band-pass filter with the capacitance reactance  $X$  and the BW= 50MHz

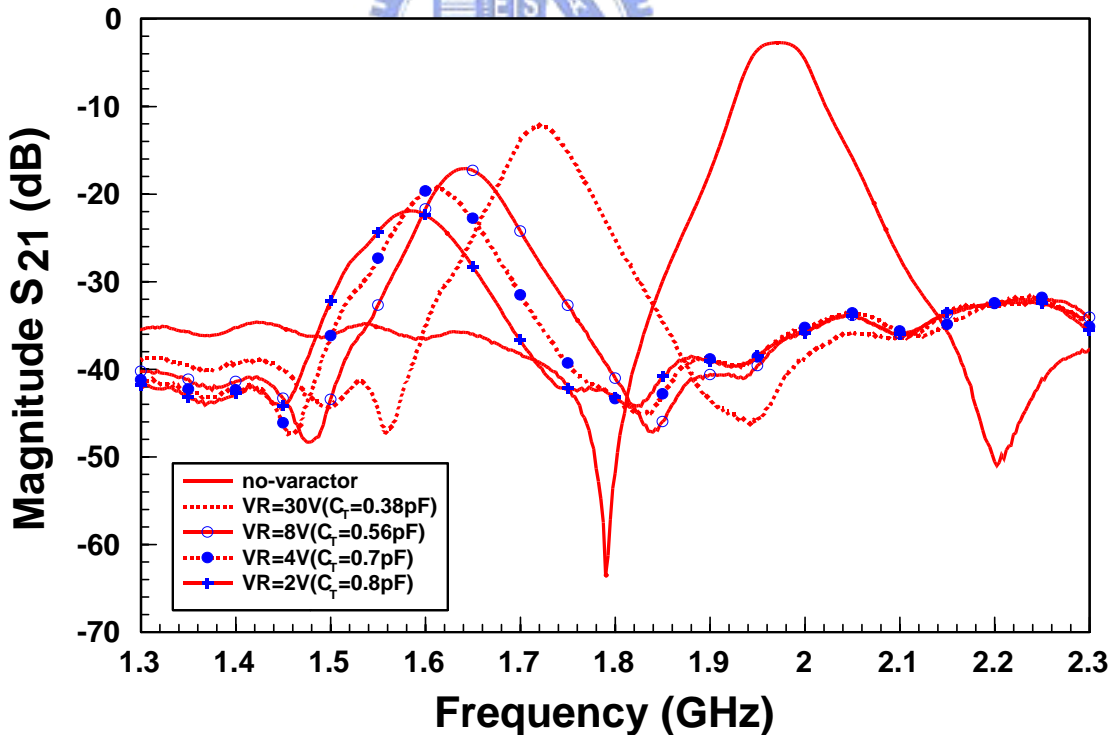
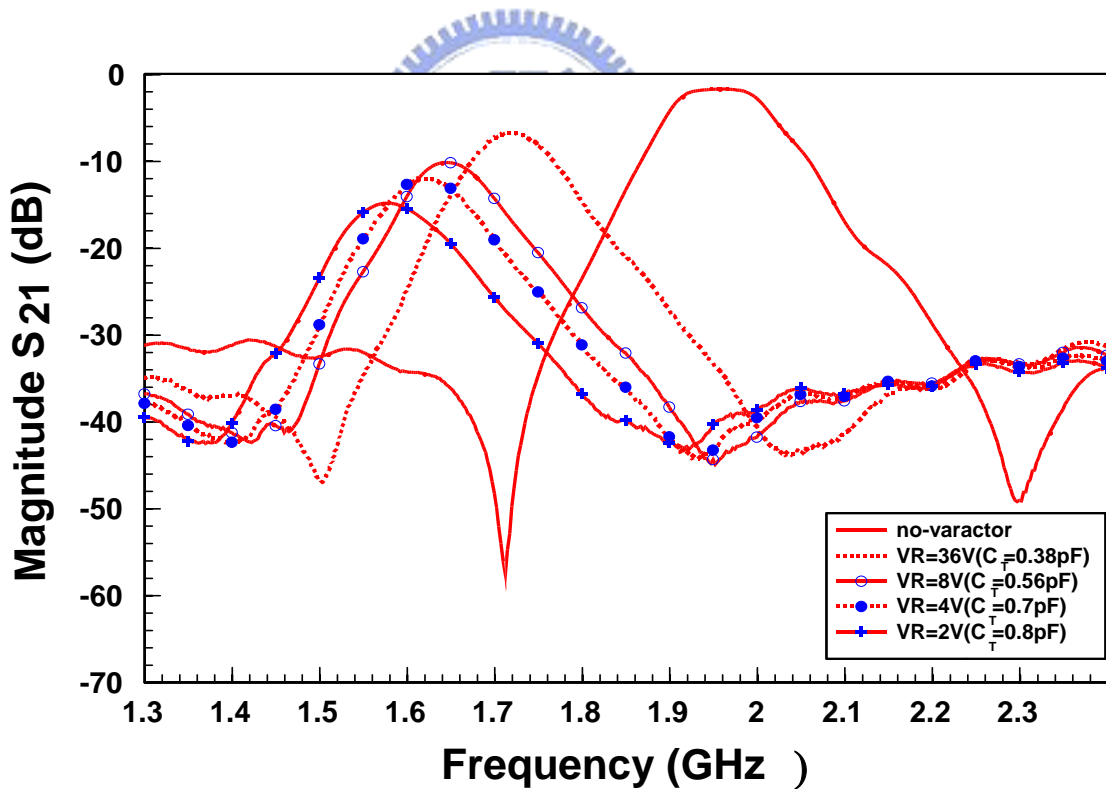


Figure 5.9 The measurement of the tunable band-pass filter with the capacitance reactance  $X$  and the BW= 50MHz

From Figure 5.8 and Figure 5.9 we can find that the tuning mechanism works when the varactor is present. Beside, we can also find the measured insertion loss is much more than that of simulated case. It should be noted that the resistor is neglected in the circuit simulation. Thus, we may infer that the loss is majorly due to the resistance, shown in Figure 5.2 (a). On the other hand, Figure 5.10 is the simulated result of the filter when the bandwidth is changed to 100MHz ( $t=3.5\text{mm}$ ,  $S=0.45\text{mm}$ ). From this figure, we can find that the insertion loss is decreased by increasing its bandwidth. In order to compare the relations among  $f_0$ ,  $C_T$ ,  $X$ ,  $BW$ ,  $V_R$  and  $S_{21}$ , we arrange the results of the simulation and measurement as listed in table 5-1.



**Figure 5.10** The measurement of the tunable band-pass filter with the capacitance reactance  $X$  and the  $BW=100\text{MHz}$

**Table 5-1** The simulation and measurement results of the tunable band-pass filter with the capacitance reactance  $X$

	$V_R(V)$	$C_T(pF)$	$X(\Omega)$	$f_0(GHz)$	$S_{21} (dB) (BW=50MHz)$	$S_{21} (dB) (BW=100MHz)$
Simulation	NONE	NONE	NONE	1.99	-2.5	-1.32
measurement				1.97	-2.69	-1.683
Simulation	30	0.38	-181.76	1.846	-2.79	-1.52
measurement				1.72	-12.197	-6.698
Simulation	8	0.56	-114.46	1.778	-3	-1.698
measurement				1.643	-17.06	-10.088
Simulation	4	0.7	-86.04	1.726	-3.17	-1.81
measurement				1.61	-19.32	-12.098
Simulation	2	0.8	-71.83	1.69	-3.31	-1.93
measurement				1.59	-21.89	-14.988

Further, it should be mentioned that the resonant frequency not only depends on  $X$  but also on  $d_1$  in the Figure 5.3. Figure 5.11 is the variation of  $d_1$  versus the resonant frequency. That is, in addition to the reactance of the varactor, the distance  $d_1$  can also provide an extra parameter for tuning the resonant frequency.

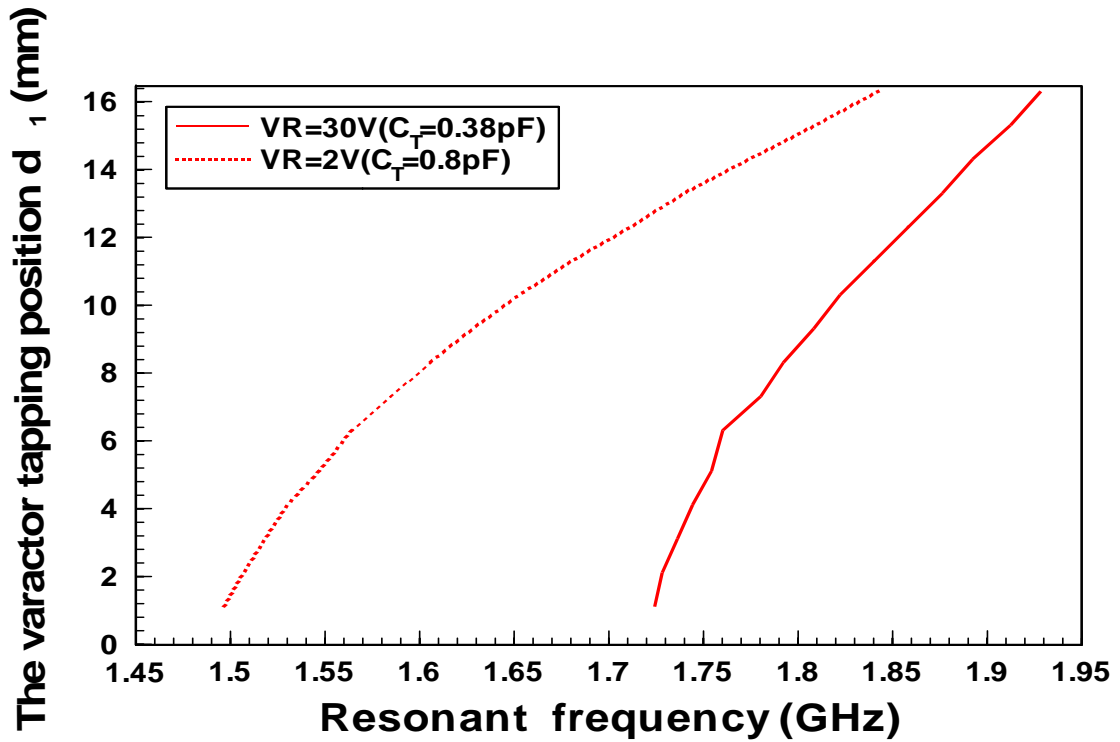
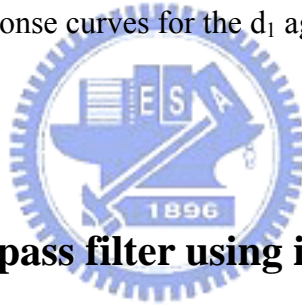


**Figure 5.11** The response curves for the  $d_1$  against the resonant frequency



### 5.3 The tunable band-pass filter using inductance reactance X

We fabricate practice a tunable band-pass filter using inductance reactance X in this chapter. In the design we use the substrate (RO4003C), the varactor LRC (BAT54RLT1), the resonant frequency of the ring resonator without varactor is 3.3 GHz ( $\lambda_0/2=28.7\text{mm}$ ), BW=150MHz,  $t=2\text{mm}$ ,  $S=0.5\text{mm}$ ,  $g=0.5\text{mm}$  and the varactor tapping position  $d_1=6.5\text{mm}$ . Similarly we find the  $L_T$  by resonant circuit first. When  $C_T=2\text{pF}$  (reverse bias  $V_R=30\text{V}$ ), by the measured  $S_{21}$  of Figure 5.4, the series LC resonant frequency  $f=2.8375\text{GHz}$ , and by equation (5.1) we can find the  $L_T=1.57\text{nH}$ . Because the capacitance on the varactor was varied from 2 to 14 pF ( $V_R$  was varied from 30 to 0 V), so the X was varied from 8.43 to 29.1



The same as section 5.3, if we find the response curves for resonant frequency  $f_0$  versus  $C_T$  and  $X$ , we can design a tunable band-pass filter whose fundamental frequency can be varied from 4.333 GHz to 4.646 GHz. The insertion loss from simulation and measurement are presented in Figure 5.12 and Figure 5.13 respectively. In order to understand the relations among  $f_0$ ,  $C_T$ ,  $X$ ,  $V_R$  and  $S_{21}$ , we arrange the results of the simulation and measurement as shown in table 5-2. From these results, we can find that the center frequencies after tuning always are greater than that without varactor. The characteristic of this filter contradicts the one shown in last section.

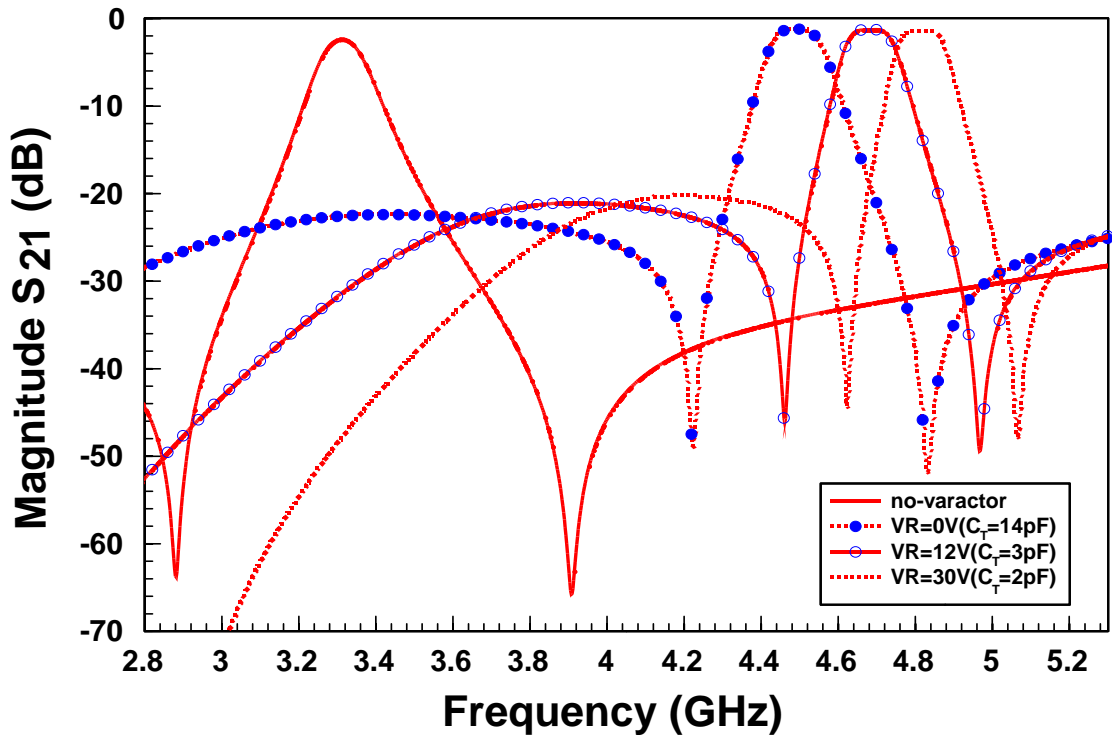


**Figure 5.12** The simulation of the tunable band-pass filter with the inductance reactance  $X$

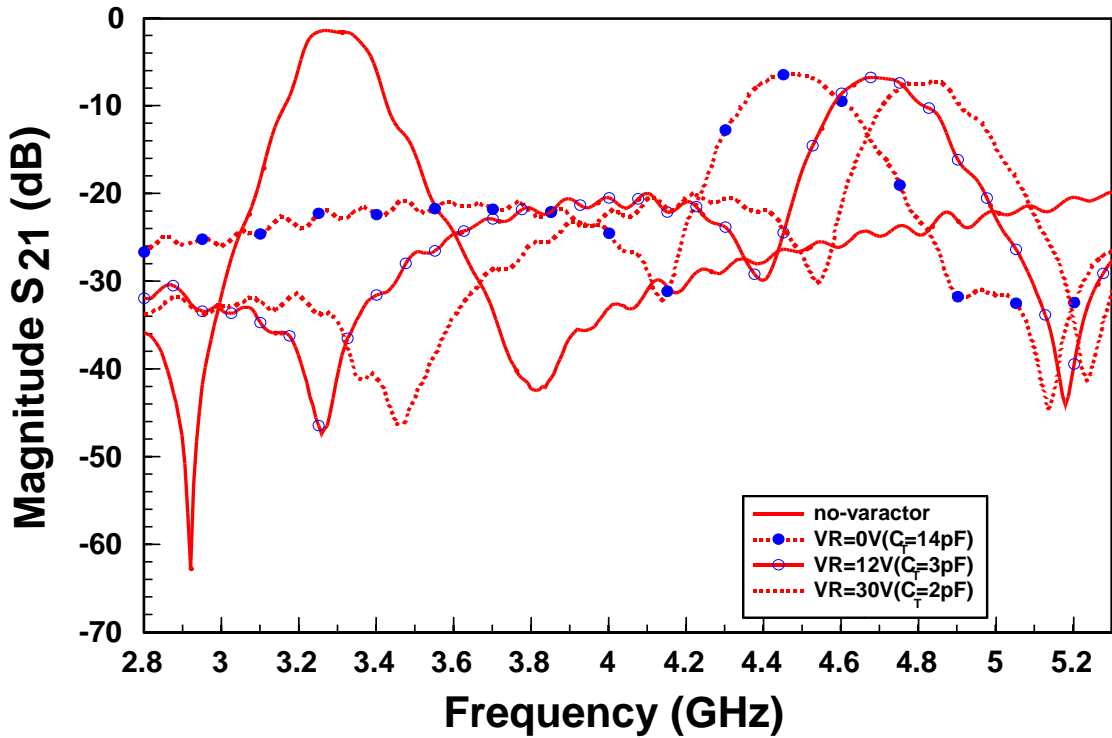


Figure 5.13 The measurement of the tunable band-pass filter with the inductance reactance X

Table 5-2 The simulation and measurement results of the tunable band-pass filter with the inductance reactance X

	$V_R$ (V)	$C_T$ (pF)	$X(\ )$	$f_0$ (GHz)	$S_{21}$ (dB)
Simulation	NONE	NONE	NONE	3.3	-2.0
measurement				3.27	-1.5
Simulation	0	14	29.1	4.48	-1.21
measurement				4.47	-6.48
Simulation	2	3	16.47	4.68	-1.29
measurement				4.71	-6.97
Simulation	30	2	8.43	4.816	-1.39
measurement				4.847	-7.34

## 5.4 The band-pass filter having wide tunable bandwidth

In the previous section, we have introduced a new circuit scheme for tuning the center frequency by using varactors. Where in the  $C_T$  and  $L_T$  determine the values of reactance  $X$ . Moreover, the positive sign of  $X$  makes the center frequency shift toward higher end; on the contrary, the center frequency shifts toward lower frequency as the sign of  $X$  is negative.

As a result, if we can change the reactance  $X$  from positive to negative value, we could have a wider tunable band-pass filter than the one described previously. Besides, the bandwidth of tuning depends not only on the range of reactance  $X$ , it is also dependent on the value of  $C_T$  (when  $L_T$  is fixed). However, the usage of a varactor having wide range of  $C_T$  is not cost-effective in such a type of circuit design.

Now we will use the similar theory but the dissimilar way to design a wideband tunable band-pass filter such as Figure 5.14, where  $N$  is the diode numbers on each branch of the ring (namely, when  $N=1$ , the total diode numbers in this tunable filter are four). The diode in this circuit is regarded as a switch. In order to design conveniently, the equivalent circuit in Figure 5.2 (b) can substitute for the switch OFF, and the short circuit can substitute for the switch ON. Now we consider the circuit in Figure 5.14 ( $N=1$ ). When the switch ON, the  $X = \omega L_T > 0$  and the frequency can be increased. On the contrary, when the switch OFF, the  $X = (-1/\omega C_T) + \omega L_T$ . The  $X < 0$  can be achieved by controlling the voltage of  $C_T$ . Therefore, this filter can have two states of center frequency.

In the design we use the substrate (RO4003C), ON SEMICONDUCTOR (BAV70LT1) diode serves as a switch, the resonant frequency of the ring resonator without varactor is 3.3 GHz ( $\lambda_0/2=28.7\text{mm}$ ), BW=150MHz,  $t=2\text{mm}$ ,  $S=0.5\text{mm}$ ,  $g=0.5\text{mm}$  and the varactor tapping position  $d_1=5\text{mm}$ . Similarly we find the  $L_T$  by Figure 5.4 circuit first. When  $C_T=0.5\text{pF}$  (diode OFF), by measuring  $S_{21}$  in Figure 5.4, the series LC resonant frequency  $f=6.2\text{GHz}$ , and from

equation (5.1) we can find the  $L_T=1.3nH$ . Figure 5.15 and Figure 5.16 are the results obtained from simulation and the measurement, respectively. Similarly, in order to obtain the relations among  $f_0$ ,  $C_T$ ,  $X$ ,  $V_R$  and  $S_{21}$ , we arrange the results of the simulation and measurement as listed in table 5-3. By the Figure 5.15 and Figure 5.16, the filter has two frequency states controlled by the switch ON and OFF. We may infer that, the filter will have  $2^N$  states of frequency, if  $N$  switches are tapped on each branch of the ring. Beside, in table 5-3 we can find that, because the frequency can be shift up and down, the filter has wide tunable frequency range. However, because the  $Q$  of the switches (diode) is not good, the insertion loss in practice is greater than that of the simulation, which again confirms the previous experiments.

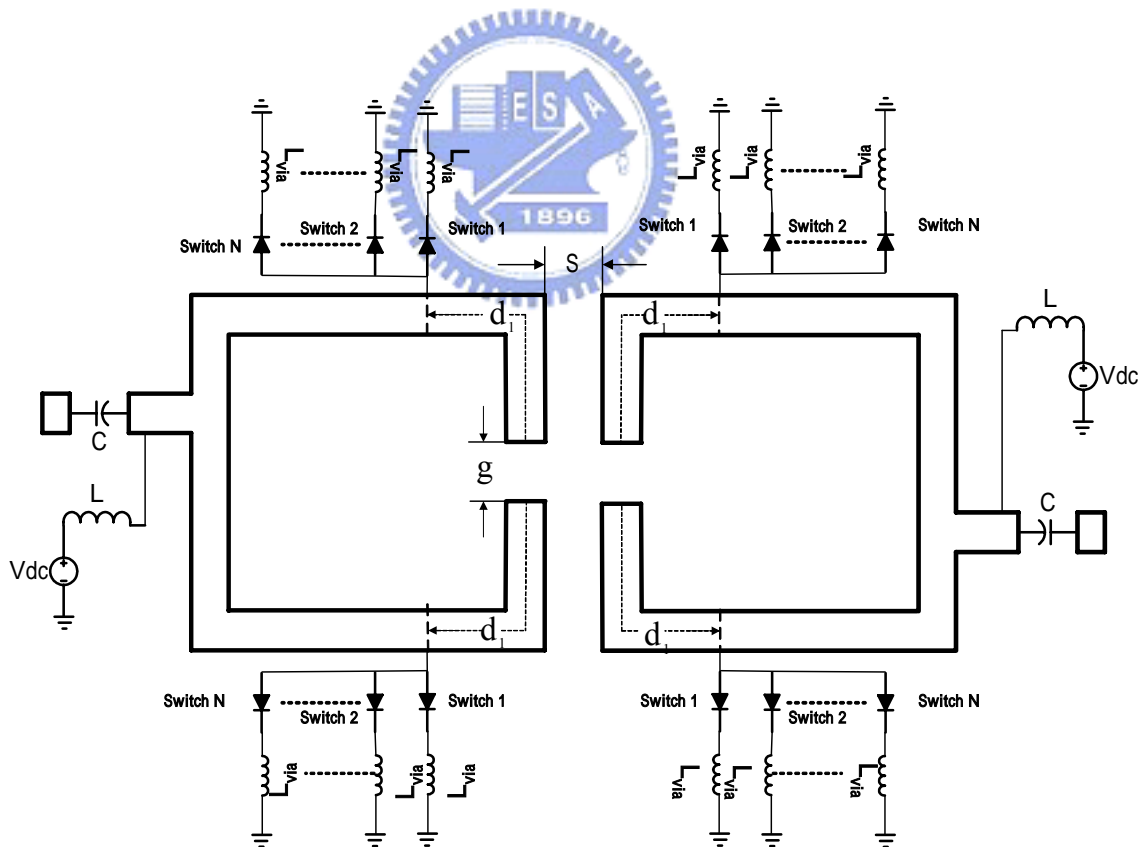


**Figure 5.14** The circuit of the band-pass filter having wide tunable bandwidth with  $N$  switches of each branch of the ring

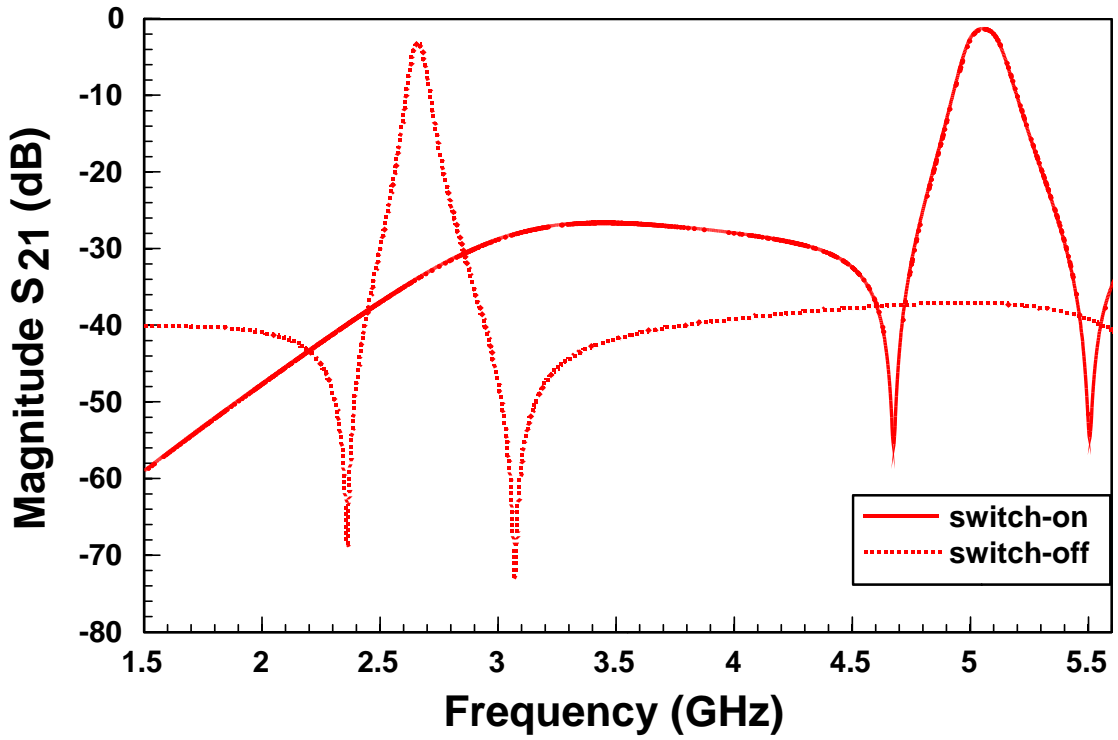


Figure 5.15 The simulation of the band-pass filter having wide tunable bandwidth for one switch of each branch of the ring

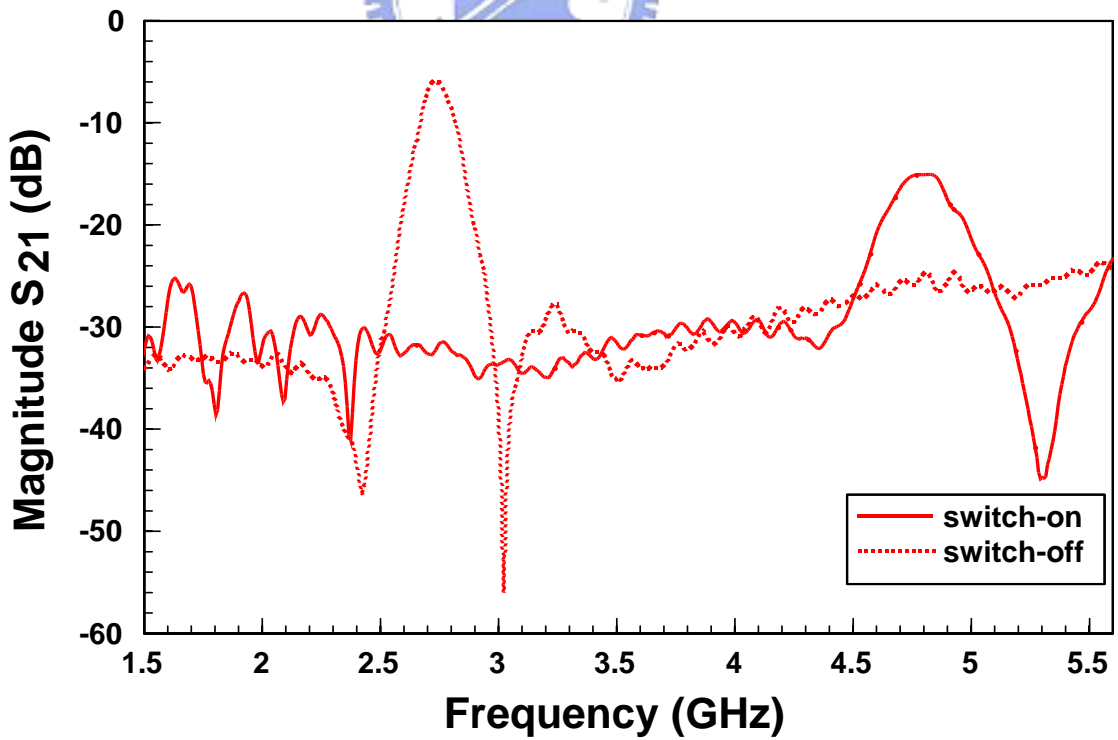


Figure 5.16 The measurement of the band-pass filter having wide tunable bandwidth for one switch of each branch of the ring

**Table 5-3** The simulation and measurement results of the tunable band-pass filter for one switch of each branch of the ring

	Switch-state	$C_T$ (pF)	$X(\ )$	$f_0$ (GHz)	$S_{21}$ (dB)
Simulation	NONE	NONE	NONE	3.3	-2.0
measurement				3.27	-1.5
Simulation	On	0	26.95	5.05	-1.36
measurement				4.8	-15.1
Simulation	Off	0.5	-69.5	2.65	-3.723
measurement				2.73	-5.94

In this chapter we proposed a new method that can tune the resonant frequency of the open loop ring resonator. We applied this method to design and fabricate some tunable band-pass filters. They include a filter whose frequency can be tuned downward, a filter whose frequency can be tuned upward, and a wide tunable frequency filter. The advantage of the new filter is that the size of the circuit is compact and the tunable frequency range is wide and, because the filters use the asymmetric feed lines, the filters have a higher selectivity. Beside, by the tapping position of the varactor or switch, the filters have another advantage is that the filters can compensate that the values of  $C_T$  and  $L_T$ , thus, it provides many possibilities in choosing devices for the filter design. However, in our proposed filters, because the Q factor of the devices is limited, the insertion losses of the filters are obvious. Some methods of the compensation for insertion loss are referred in [16][9]. These methods can also be applied to the tunable filters for our design.

# Chapter 6

## Conclusion

In this thesis, a new scheme of tunable band-pass filter was proposed and implemented. The varactor was employed to adjust the reactance and what follows is the resonant frequency of the band-pass filter. In addition to the reactance provided by the varactor, the position where the varactor is added is also a parameter in conjunction with the overall performance of the filter. However, since the quality factor of this diode is not considerable, the insertion loss becomes obvious and then degrades its performance. This drawback could be overcome by introducing negative resistor or etc, and may be a good research topic in the future.



# Reference

- [1] G. L. Matthaei, L. Young, and E. M. T. Jones, "Microwave Filters, Impedance-Matching Networks, and Coupling Structures." New York: McGraw-Hill, 1980, ch. 11.
- [2] Jia-Sheng Hong, Michael J. Lancaster, "Couplings of Microstrip Square Open-Loop Resonators for Cross-Coupled Planar Microwave Filters," IEEE Trans Microwave Theory and Techniques, vol. 44, NO. 12, December 1996.
- [3] K. T. Jokela, "Narrow-band stripline or microstrip filters with transmission zeros at real and imaginary frequencies," IEEE Trans. Microwave Theory Tech., vol. MTT-28, pp. 542-547, June 1980.
- [4] S. Y. Lee and C. M. Tsai, "New cross-coupled filter design using improved hairpin resonators," IEEE Trans. Microwave Theory Tech., vol. 48, pp. 2482-2490, Dec. 2000.
- [5] L. H. Hsien and K. Chang, "Tunable Microstrip Bandpass Filters With Two Transmission Zeros" IEEE Trans. Microwave Theory Tech., vol. 51, pp. 520-525, February 2003.
- [6] J. Uher, J. R. Hoelfer, "Tunable Microwave and Millimeter-Wave Band-Pass Filters," IEEE MTTs, vol. 39, no. 4 April 1991
- [7] S. Kumar, D. Klymyshyn and A. Mohammadi, "broadband electronically tunable microstrip ring resonator filter with negative resistance coupling" IEEE Letters Vol. 32, no 9, pp. 809-810, 25th April 1996
- [8] M. Makimoto and M. Sagawa, "Varactor Tuned Bandpass Filters Using Microstrip-Line Ring Resonators," IEEE MTT-s, pp. 411-414, 1986
- [9] A. Cenac, L. Nenert, L. Billonnet, B. Jarry, P. Guillon, "Broadband Monolithic Analog Phase Shifter and Gain Circuit For Frequency Tunable Microwave Active Filters," IEEE MTT-S Dig., Volume: 2, 7-12, Pages:869 - 872 vol.2, June 1998



- [10] X. P. Liang, Y Zhu, “Hybrid Resonator Microstrip Line Electrically Tunable Filter,” IEEE MTT-S D, Volume: 3, 20-25 Pages: 1457 - 1460, May 2001
- [11] M. Makimoto, M. Sagawa, “Varactor Tuned Bandpass Filters Using Microstrip-Line Ring Resonators,” IEEE MTT-S, Volume: 86, Issue: 1, 2 Pages: 411 – 414, Jun 1986
- [12] David M. Pozar, “Microwave Engineering,” John Wiley & Sons, Inc., 1998
- [13] Kai Chang, Jia-Sheng Hong, M. J. Lancaster, “Microstrip Filters for RF/Microwave Applications,” John Wiley & Sons, Inc. 2001
- [14] R. Garg and I. J. Bahl, “Microstrip discontinuities,” Int. j. Electron., vol. 45, pp. 81-87, July 1978.
- [15] Kai, Chang, “Microwave Ring Circuits and Antennas,” John Wiley & Sons, Inc. 1996
- [16] D. K. Paul, M. Michael and K. Konstantinou, “MMIC Tunable Bandpass Filter Using A Ring Resonator With Loss Compensation,” IEEE MTT-s Digest, Volume: 2, 8-13 Pages: 941 - 944 vol.2 June 1997



# Appendix A

Element values for Butterworth low-pass filter prototypes ( $g_0=1$ ,  $L_{Ar}=3.01\text{dB}$  at  $\omega_c=1$ ,  $n=1$  to 10)

n	$g_1$	$g_2$	$g_3$	$g_4$	$g_5$	$g_6$	$g_7$	$g_8$	$g_9$	$g_{10}$	$g_{11}$
1	2.0000	1.0000									
2	1.4142	1.4142	1.0000								
3	1.0000	2.0000	1.0000	1.0000							
4	0.7654	1.8478	1.8478	0.7654	1.0000						
5	0.6180	1.6180	2.0000	1.6180	0.6180	1.0000					
6	0.5176	1.4142	1.9318	1.9318	1.4142	0.5176	1.0000				
7	0.4450	1.2470	1.8019	2.0000	1.8019	1.2470	0.4450	1.0000			
8	0.3902	1.1111	1.6629	1.9615	1.9615	1.6629	1.1111	0.3902	1.0000		
9	0.3473	1.0000	1.5321	1.8794	2.0000	1.8794	1.5321	1.0000	0.3473	1.0000	
10	0.3129	0.9080	1.4142	1.7820	1.9754	1.9754	1.7820	1.4142	0.9080	0.3129	1.0000

